

1 **Future permafrost degradation under climate change in a headwater catchment of Central**
2 **Siberia: quantitative assessment with a mechanistic modelling approach**

3 Thibault Xavier¹, Laurent Orgogozo^{1*}, Anatoly S. Prokushkin², Esteban Alonso-González³, Simon
4 Gascoin⁴, Oleg S. Pokrovsky^{1,5}

5 ¹Geoscience Environnement Toulouse (GET), CNRS, UMR5563, Toulouse, 31400, France

6 ²V.N. Sukachev Institute of Forest SB RAS, Russia

7 ³Instituto Pirenaico de Ecología, Consejo Superior de Investigaciones Científicas (IPE-CSIC), Jaca,
8 Spain

9 ⁴Centre d'Etudes Spatiales de la Biosphère, Université de Toulouse, CNRS/CNES/IRD/INRA/UPS,
10 Toulouse, France

11 ⁵BIO-GEO-CLIM Laboratory, Tomsk State University, Tomsk, Russia

12 * *Corresponding author*: Laurent Orgogozo (laurent.orgogozo@get.omp.eu)

13 **Abstract**

14 Permafrost thawing as a result of climate change has major consequences locally and globally for
15 the biosphere as well as for human activities. The quantification of its extent and dynamics under
16 different climate scenarios is needed to design local adaptation and mitigation measures and to
17 better understand permafrost climate feedbacks. To this end, numerical simulation can be used to
18 explore the response of soil thermal and hydrological regimes to changes in climatic conditions.
19 Mechanistic approaches minimise modelling assumptions by relying on the numerical resolution of
20 continuum mechanics equations, but they involve significant computational effort. In this work, the
21 permaFoam solver is used along with high-performance computing resources to assess the impact
22 of four climate scenarios of the Coupled Model Intercomparison Project Phase 6 (CMIP6) on
23 permafrost dynamics within a pristine, forest-dominated watershed in the continuous permafrost
24 zone. Using these century time-scale simulations, changes in the soil temperature, soil moisture,
25 active layer thickness and water fluxes are quantified, assuming no change in the vegetation cover.
26 The most severe scenario (SSP5-8.5) suggests a dramatic increase in both the active layer thickness
27 and annual evapotranspiration, with the maximum values on the watershed in 2100 increasing by
28 +65% and +35% compared to current conditions, respectively. For the active layer thickness, a
29 variable that integrates both the thermal and hydrological states of the near-surface permafrost, this
30 projected increase would correspond to a ~350 km southward shift in current climatic conditions.
31 Moreover, in this scenario, the thermal equilibrium of near-surface permafrost with the new
32 climatic conditions would not be reached in 2100, suggesting a further thawing of permafrost even
33 in the case in which the climate change is halted.

34 **Keywords**

35 Permafrost, climate change, boreal forest, numerical modelling, high performance computing, soil
36 temperature, soil moisture, evapotranspiration.

37

38 **1 Introduction**

39

40 Permafrost is mostly situated in regions that are experiencing especially intense climate
41 change, resulting in widespread warming and thawing, with the shrinking of its lateral extent and
42 the thickening of the soil active layer (Biskaborn et al., 2019; Hu et al., 2022; Li et al.; 2022a, b).
43 Permafrost thawing induces sizable changes in the environment (Walvoord and Kurylyk, 2016;
44 Nitze et al., 2018; Makarieva et al., 2019; Jin et al., 2022; Wright et al., 2022) and for human
45 activities (Shiklomanov et al., 2017; Strelestkiy et al., 2019, 2023; Hjort et al., 2018, 2022) in the
46 Arctic and the sub-Arctic. For instance, a permafrost-thaw-related decrease in the soil moisture
47 leads to an increase in boreal fire frequency (Kurylyk, 2019; Kim et al., 2020), while soil
48 mechanical instabilities induced by permafrost thawing threaten human settlements (Ramage et al.,
49 2021) and infrastructure (Bartsch et al., 2021). Moreover, permafrost thaw may exert significant
50 controls on the biogeochemical cycles of carbon and related metals (Sonke et al., 2018; Karlsson et
51 al., 2021; Walvoord and Striegl, 2021) and climate dynamics (Miner et al., 2022; Park and Kug,
52 2022; de Vrese et al., 2023), with potentially major feedback on climate warming. Thus,
53 anticipating the evolution of permafrost cover and dynamics is of primary importance for
54 understanding and mitigating the climate-change-induced impacts at high latitudes. For this, robust
55 and accurate numerical simulations are required (Schneider von Deimling et al., 2022; Hu et al.,
56 2023).

57 Boreal forest is one of the largest biomes on Earth (Gauthier et al., 2015), and 80% of its
58 area is located in permafrost regions, where it covers 55% of the territory (Stuenzi et al., 2021).
59 Due to the complexity of the biophysical processes involved, quantifying the evolution of
60 permafrost dynamics in boreal forests under climate change requires mechanistic, high-resolution
61 modelling approaches (Orgogozo et al., 2019). However, the large extent of the considered areas
62 makes the use of such approaches impracticable at global, continental or regional scales. As a
63 consequence, the mechanistic modelling of permafrost dynamics has to focus on processes at the
64 watershed scale in headwater catchments with long-term environmental monitoring, following a

65 general trend in the Arctic sciences (Speetjens et al., 2023; Vonk et al., 2023). In Arctic
66 environments, the vegetation strongly controls the surface energy budget (Fedorov et al., 2019;
67 Oehri et al., 2022), interacts with climate dynamics (Park et al., 2020; Kirilyanov et al., 2024) and
68 drives water fluxes (Orgogozo et al., 2019). As such, vegetation should be taken into account when
69 simulating the impact of climate warming on permafrost in boreal forest areas (Lorant et al., 2018,
70 Kirilyanov et al., 2020; Holloway et al., 2020).

71 The quantitative mechanistic modeling of permafrost dynamics under climate change at the
72 headwater catchment scale requires large computational resources, because fine spatio-temporal
73 discretization is needed due to the strong non-linearities and couplings of various physical processes
74 (Kurylyk and Watanabe, 2013). This is especially important for century long simulation periods
75 (O'Neill et al., 2016) and simulation domains with surfaces of up to tens of square kilometres (e.g.
76 Arndal and Torp-Jørgensen, 2020). For this, high performance computing techniques are needed
77 (Orgogozo et al., 2023).

78 In this study, we focus on a permafrost-dominated, forested watershed of central Siberia that
79 was subjected to long-term environmental monitoring, the Kulingdakan watershed (e.g. Prokushkin
80 et al., 2007; Mashukov et al., 2021). The objective is to assess the future state of the permafrost and
81 the ground thermal regime in this continuous-permafrost, boreal forest environment under different
82 climate change scenarios at the century time scale. The permafrost status of this catchment under
83 current climatic conditions has already been investigated (Orgogozo et al., 2019). Here, we
84 simulate, using a mechanistic modelling approach, the permafrost dynamics at the catchment scale
85 until 2100 under various scenarios of climate change. The vegetation controls on permafrost
86 dynamics are partly included in the mechanistic modelling framework, considering
87 evapotranspiration fluxes (Orgogozo et al., 2019), and partly handled empirically, via accounting
88 for the insulating effect of ground-floor vegetation (Blok et al., 2011; Cazaurang et al., 2023).
89 However, because no changes in vegetation are explicitly considered, we assume constant biomass
90 and primary production and therefore investigate only the physical part of the response of
91 permafrost to climate change. We use the permaFoam high performance computing
92 cryohydrogeological simulator (Orgogozo et al., 2023) with a national-level supercomputing
93 infrastructure, the Joliot-Curie supercomputer of the Très Grand Centre de Calcul (TGCC) of the
94 French Alternative Energies and Atomic Energy Commission (CEA). The simulated permafrost
95 thawing features in Kulingdakan are discussed and compared for different CMIP6 scenarios,
96 including the following:

- 97 - the soil thermal regime (soil temperature and active layer thickness evolution, equivalent
- 98 southward shift under current climatic conditions);
- 99 - the soil hydrology (evapotranspiration fluxes and soil moisture evolution);
- 100 - the spatial variability of climate warming impacts at the scale of the watershed under study;
- 101 - the state and evolution of the thermal imbalance of the permafrost (e.g. Ji et al., 2022; Nitzbon et
- 102 al., 2023) in the considered region.

103 **2 Materials and methods**

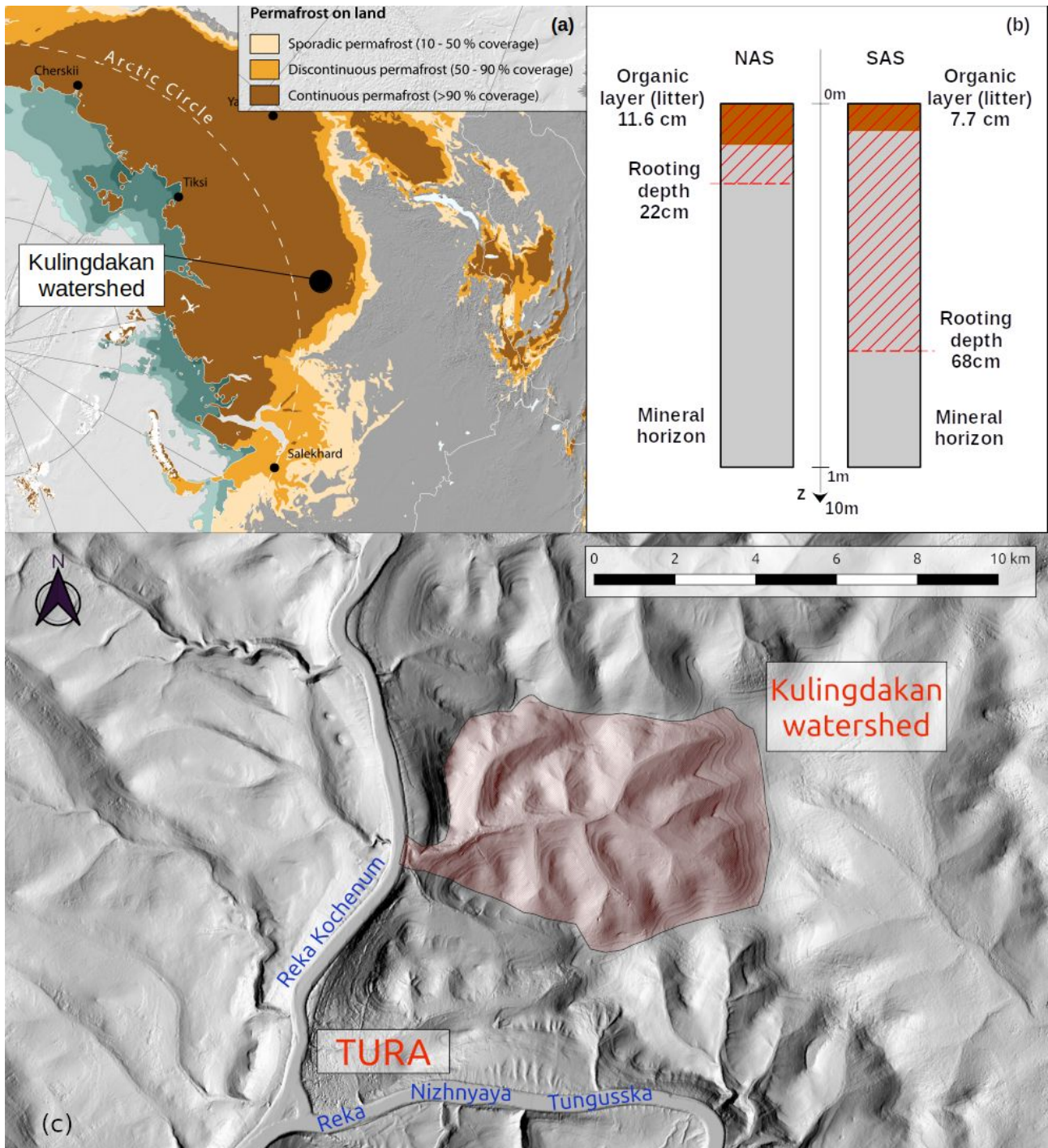
104 **2.1 Study site: Kulingdakan, a forested catchment in continuous-permafrost area**

105 The Kulingdakan catchment is located in the Krasnoïarsk region (64.31°N, 100.28°E),
106 within a continuous permafrost zone, belonging to the boreal forest biome (Northern Taïga – see
107 Fig. 1a). This pristine catchment has been monitored for the study of boreal processes over the past
108 two decades. The vegetation is dominated by larch (*Larix gmelinii*), dwarf shrubs, mosses and
109 lichens. The catchment covers an area of 41 km² and has an elevation ranging from 132 m to 630 m
110 (Prokushkin et al., 2004). The climate is cold and continental, with an average annual mean
111 temperature of -8°C and an annual total precipitation of 400 mm (annual mean measured between
112 1999 and 2014 at the Tura meteorological station, 5 km south of the Kulingdakan catchment,
113 altitude of 168 m). The stream, which flows from east to west, divides the 41 km² catchment area
114 into two approximately rectangular slopes of equal area, the North Aspect Slope (NAS) and the
115 South Aspect Slope (SAS). As shown by a previous numerical study using permaFoam of this site
116 under current climatic conditions, the hydrological budget in this watershed is largely dominated by
117 evapotranspiration fluxes (Orgogozo et al., 2019). Two horizons constitute the soil in the first few
118 metres: an organic horizon (litter and peat) and a mineral horizon (mainly rocky/gravelly loam).

119 Due to the difference in solar radiation induced by their aspects, primary production and
120 evapotranspiration are more intensive in the SAS than in the NAS. Thus the two slopes show
121 significant differences in the larch tree size and larch stand density, as well as in the rooting depth,
122 organic horizon and moss layer thickness and active layer dynamics. The thickness of the organic
123 horizon is 11.6 cm on the NAS and 7.7 cm on the SAS (Gentsch, 2011), while the moss layer
124 thickness is 13 cm on the NAS and 6.4 cm on the SAS (Prokushkin et al., 2007). The rooting depth
125 is 10 cm into the mineral horizon for the NAS and 60 cm for the SAS (Viers et al., 2013), and this
126 difference has been shown to be of great importance for the dynamics of the active layer (Orgogozo
127 et al., 2019). The observed maximum active layer thickness is 1.22 m in the SAS and 0.58 m in the

128 NAS (Gentsch, 2011). These pedological and physiological contrasts between the two aspects of the
 129 watershed slope, summarised in Figure 1b, are explicitly considered when performing permafrost
 130 simulations (Supplementary Material B).

131



132 **Figure 1: (a) Location of Kulingdakan watershed (map from GRID-Arendal/Nunataryuk). (b)**
 133 **Representation of soil column structure for North Aspected Slope (NAS) and South Aspected**

134 **Slope (SAS) of the Kulingdakan watershed. (c) Digital Elevation Model (DEM) of**
 135 **Kulingdakan watershed, extracted from ArcticDEM (Porter et al., 2023).**

136 Previous modelling studies in the Kulingdakan catchment on water flux repartition, the soil
 137 temperature at different depths and the active layer thickness (Orgogozo et al., 2019; Orgogozo et
 138 al., 2023) demonstrated that the use of the permaFoam solver, together with boundary conditions
 139 (water fluxes and soil surface temperature) provided by field measurements, made it possible to
 140 obtain numerical simulation results in agreement with in-situ observations under current climatic
 141 conditions .

142 **2.2 The permaFoam cryohydrogeological simulator**

143 The numerical tool used in this study is permaFoam (Orgogozo et al., 2019, 2023), the
 144 permafrost modelling solver developed in the framework of OpenFOAM, the open source, high
 145 performance computing tool box for computational fluid dynamics (Weller et al., 1998,
 146 openfoam.org, openfoam.com). This solver is designed to simulate 3D, transient coupled heat and
 147 water transfers in a variably saturated soil with evapotranspiration and the freezing/thawing of the
 148 pore water. The two main equations solved by permaFoam are the Richards equation (Eq. (1)),
 149 which governs the flow of water, and an energy balance equation (Eq. (2)) that governs the heat
 150 transfer; both are defined at the Darcy scale of the considered porous medium (soil):

151

$$C_H(h) \frac{\partial h}{\partial t} = \nabla \cdot (K_H(h, T) \cdot \nabla (h+z)) + Q_{AET}(h, t) \quad (1)$$

$$\frac{\partial \left(\left(C_{T,eq}(h, T) + L \frac{\partial \theta_{ice}(h, T)}{\partial T} \right) T \right)}{\partial t} + \nabla \cdot (V(h, T) C_{T,liquid} T) = \nabla \cdot (K_{T,eq}(h, T) \nabla T) \quad (2)$$

152

153 The two primary variables in Eqs, (1) and (2) are the generalised water pressure head h [m] and the
 154 soil temperature T [K], respectively. In the Richards equation (Eq. (1)), z is the vertical coordinate
 155 [m] (oriented upward), K_H is the hydraulic conductivity of the variably saturated, variably frozen
 156 porous medium [$m \cdot s^{-1}$], C_H is the capillary capacity (also called the specific moisture capacity) of
 157 the unsaturated porous medium [m^{-1}] and Q_{AET} [s^{-1}] is a source term representing the water uptake
 158 by vegetation through the evapotranspiration process (computed using the Hamon formula; see
 159 Hamon, 1963; Frohling, 1997). From the pressure head field h , the Darcy velocity V [$m \cdot s^{-1}$] is
 160 derived according to Eq. (3):

$$V(h, T) = K_H(h, T) \cdot \nabla(h + z) \quad (3)$$

161

162 In the energy balance equation (Eq. (2)), the considered transfer processes are conduction through
 163 the entire porous medium, convection by pore water flow, and latent heat exchanges when phase
 164 change occurs. In this heat transfer equation, $K_{T,eq}$ [$J \cdot m^{-1} \cdot s^{-1} \cdot K^{-1}$] is the apparent thermal conductivity
 165 of the porous medium, θ_{ice} [-] is the volumetric ice content, L [$J \cdot m^{-3}$] is the latent heat of fusion of
 166 ice, $C_{T,eq}$ [$J \cdot m^{-3} \cdot K^{-1}$] is the equivalent heat capacity of the porous medium, and $C_{T,liquid}$ [$J \cdot m^{-3} \cdot K^{-1}$] is the
 167 equivalent heat capacity of liquid water. In permaFoam these two coupled equations are solved in
 168 3D using the finite volumes method, with sequential operator splitting for handling the couplings,
 169 Picard loops for dealing with the non-linearities and a backward time scheme for temporal
 170 discretisation. A detailed description of the solver can be found in Orgogozo et al. (2023).

171 The numerical resolution of these coupled and highly non-linear equations, including stiff
 172 fronts generated by freeze/thaw processes, at the space and time scales required for studying climate
 173 change impacts on boreal watersheds requires both a robust algorithm and the efficient use of high
 174 performance computing means. This is the reason that permaFoam is developed within the
 175 OpenFOAM framework, which allows the use of up-to-date and efficient numerical methods for
 176 solving partial differential equations on last-generation supercomputing facilities. Thanks to its
 177 implementation in OpenFOAM, the permaFoam solver has demonstrated excellent parallel
 178 performances on various supercomputer architectures for dedicated test cases (Orgogozo et al.,
 179 2023), both in terms of large numerical domains (up to 1 billion mesh points on the CALMIP
 180 Olympe supercomputer) and the number of cores (16,000 on the GENCI IRENE-ROME
 181 supercomputer).

182

183 **2.3 Modelling domain**

184 According to preliminary numerical experiments (data not shown), for modelling
 185 Kulingdakan watershed permafrost the use of a dual 2D simplified representation (Orgogozo et al.,
 186 2019) makes it possible to simulate properly the thermal and hydrological fluxes in the soils. As
 187 such, full 3D simulations, which are far more costly from a computational perspective than 2D
 188 simulations (Orgogozo et al., 2023), are not needed. Additionally, the use of 2D simulations allows
 189 the consideration of lateral transfers (Sjöberg et al., 2016; Lamontagne-Hallé et al.; 2018, Hamm
 190 and Frampton, 2021; Jan, 2022). Thus, in this work we used 2D numerical domains, with climatic

191 forcing as the top boundary conditions (see section 2.4) and geothermal heat flux and nil water flux
192 as the bottom boundary conditions. The initial conditions were obtained by 10 years of spin-up
193 under current climatic conditions. These current climatic conditions were represented by a synthetic
194 year of climate forcing corresponding to the multi-annual means of the 1999–2014 observations
195 (see Supplementary Material A, including Fig. S1). The starting conditions of this spin-up were
196 extracted from the results of the previous calculations (Orgogozo et al., 2019). The convergence
197 criterion for the spin-up was the active layer thickness inter-annual difference (annual variability
198 less than 0.2%). The spatial discretisation of the domain is done using a mesh of 5.2×10^7 cells,
199 according to a convergence study presented in Supplementary Material B.

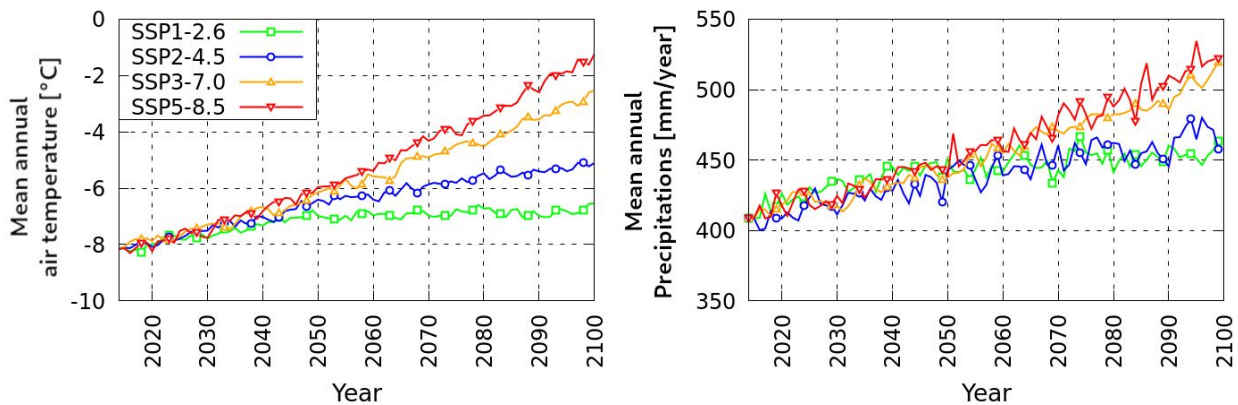
200 The numerical simulations provide the full 2D fields of physical quantities describing the
201 heat and water flow within both the SAS and NAS (two 2.5-km-wide, 10-m-thick slopes), including
202 both the frozen and active layers in each slope. These included the soil temperature, pressure head,
203 liquid water content and ice content for each time step that was saved (user defined; here, every 6
204 months). In addition, the temperature, water content, ice content and evapotranspiration sink term
205 are monitored at an hourly frequency throughout two vertical profiles located at the mid-slope of
206 the SAS and NAS numerical domains, using 61 virtual point probes distributed over the 10 m of the
207 numerical domain thickness. Finally, the infiltration and exfiltration water fluxes through the total
208 soil surface are also saved from the standard output at every time step. Further details of modelling
209 set up are presented in Supplementary material B.

210 ***2.4 Soil surface conditions under climate change derived from CMIP6 scenarios***

211 In order to apply climate forcings that are representative of possible future trajectories, we
212 consider climate scenarios produced as a part of the Coupled Model Intercomparison Project Phase
213 6 (CMIP6) organised by the Intergovernmental Panel on Climate Change (IPCC) (Eyring et al.,
214 2016); in particular, we consider the so-called tier-1 key scenarios (O'Neill et al., 2016). These
215 scenarios have been highlighted because of their relevance to scientific questions, the range of
216 possible futures they cover, and their continuity with previous representative common pathways
217 (RCP) scenarios (van Vuuren et al., 2011) published during CMIP5. We considered four CMIP6
218 scenarios, from sustainable pathway with the least forcing (coldest) to the pathway with the most
219 forcing (hottest): SSP1-2.6, SSP2-4.5, SSP3-7.0 and SSP5-8.5. Among these scenarios, SSP2-4.5 is
220 the one most often used in permafrost studies (e.g. Karjalainen et al., 2019; Ramage et al., 2021;
221 Hjort et al., 2022). For each of these scenarios, an ensemble of models has been run on different

222 regions of the globe. The climate model output data were accessed via the IPCC Working Group I
 223 (IPCC-WGI) Interactive Atlas (Iturbide et al., 2021), February 2023 version, which provides the
 224 median (P50) of the ensemble of models for a selected output variable, region and scenarios. We
 225 used the projections of the air temperature and precipitation changes for the East Siberian region,
 226 averaged at each yearly time step. To obtain the local scenarios of climate change for the air
 227 temperature and precipitation (Fig. 2), these yearly averaged projections of air temperature /
 228 precipitation changes between 2015 and 2100 have been summed with daily air temperature /
 229 precipitation variations along the synthetic year of climate forcing corresponding to the multi-
 230 annual means of the 1999–2014 observations in Tura, which are representative of current climatic
 231 conditions (see Supplementary Material A, Fig. S1). This provided the projections of the daily air
 232 temperature / precipitation from 2015 to 2100 for the Tura area. The yearly averages of these daily
 233 projections are presented in Figure 2.

234



235

236 **Figure 2: Projections of air temperature and precipitation in Kulingdakan based on CMIP6**
 237 **projections on the Eastern Siberia area.**

238 The projections show an increase in the air temperature over the century, with a rate
 239 between $+1.9^{\circ}\text{C}/100$ years (SSP1-2.6) and $+7.8^{\circ}\text{C}/100$ years (SSP5-8.5); these rates were obtained
 240 by re-scaling the averaged increase rates from 2014 to 2100 to the centennial time scale. For every
 241 scenario this local increase rate is higher than the global one (global increase rates, according to Fan
 242 et al. [2020]: SSP1-2.6: $+1.18^{\circ}\text{C}/100$ years; SSP2-4.5: $+3.22^{\circ}\text{C}/100$ years; SSP3-7.0: $+5.50^{\circ}\text{C}/100$
 243 years; SSP5-8.5: $+7.20^{\circ}\text{C}/100$ years). The annual precipitation could also change significantly, with
 244 a relative increase in 2100 of $+12\%$ (SSP1-2.6) to $+29\%$ (SSP5-8.5) compared to the current value.

245 In order to translate these climate projections, which describe atmospheric conditions, into
 246 suitable soil surface boundary conditions for cryohydrogeological simulations (water fluxes and

247 temperature at the soil surface, beneath snow and moss layers), a dedicated empirical procedure has
248 been developed. The goal is to set up a methodology for deriving the soil surface temperature from
249 the air temperature on the slopes of the Kulingdakan watershed, based on the available observation
250 data. Indeed, the soil temperature and air temperature may be significantly different in such a boreal
251 forest environment, due to the effects of understorey (Zellweger et al., 2019; Haesen et al., 2021),
252 moss cover insulation (Blok et al., 2011; Cazaurang et al., 2023), the winter snowpack (Jan and
253 Painter, 2020; Khani et al., 2023) and its interactions with vegetation (Dominé et al., 2022). This
254 empirical, site-specific procedure is detailed in Supplementary Material A, and it makes it possible
255 to build up slope-wise soil temperature estimates on the basis of the air temperature and snow
256 conditions. For water fluxes, the simplest approximation has been adopted, assuming that the water
257 flux at the top of the soil is equal to the rain flux. For the soil surface temperature estimate, we first
258 used a modified temperature index approach (Braithwaite and Olesen; 1989, Hock 2003) for
259 estimating the snow water equivalent, and then we used multiple regression to derive below-moss
260 soil surface temperature from the air temperature, precipitation and snow water equivalent. We
261 chose a temperature index approach to simulate the snow water equivalent on the soil surface
262 because climate projections only provide the air temperature and precipitation, whereas a more
263 advanced energy balance snowpack model requires additional information on wind, radiation, and
264 air humidity. To calibrate this temperature index model we first reconstruct the snow water
265 equivalent for the period 1999–2014 from the observed snow depth with the Multiple Snow Data
266 Assimilation System (MuSA) toolbox (Alonso-González et al., 2022) forced with ERA5 data
267 (Hersbach et al., 2020), fusing available snow depth observations with an ensemble of simulations
268 generated by the energy and mass balance model called the Flexible Snow Model (Essery, 2015).
269 Then, we calibrated a multiple regression method to derive the soil surface temperature as a
270 function of the air temperature and precipitation, while taking into account the insulating effect of
271 moss and snow layers. Calibrations were performed with air temperature and precipitation data
272 measurements, the MuSA-derived snow water equivalent between 1999 and 2014 and the top-soil
273 (i.e. below moss) temperature measured in situ between 2003 and 2005. With this procedure, for
274 each slope, an empirical transfer function that provides soil temperature estimates derived from the
275 air temperature and precipitation was obtained. Finally, these transfer functions were used to
276 produce scenarios of the daily soil surface temperature under climate change for the two slopes of
277 the catchment. This information is to for build the soil surface boundary conditions of the
278 hydrogeological simulations. It must be emphasised that our empirical approach was based on

279 parametrical fitting on observation data for estimating the transfer function between atmospheric
280 forcing and the soil surface temperature. As a result, no vegetation changes due to climate change
281 could be considered in this transfer function. Therefore, we focus on the purely physical response of
282 the catchment permafrost to climate change, while considering the vegetation impacts on
283 permafrost dynamics at constant vegetation cover. Coupling a vegetation dynamics with the
284 cryohydrogeological model would allow one to assess the impact of the climate warming-induced
285 changes of the vegetation cover on permafrost conditions. However, this is beyond the scope of the
286 present study and will be the focus of future work.

287 **3 Results**

288

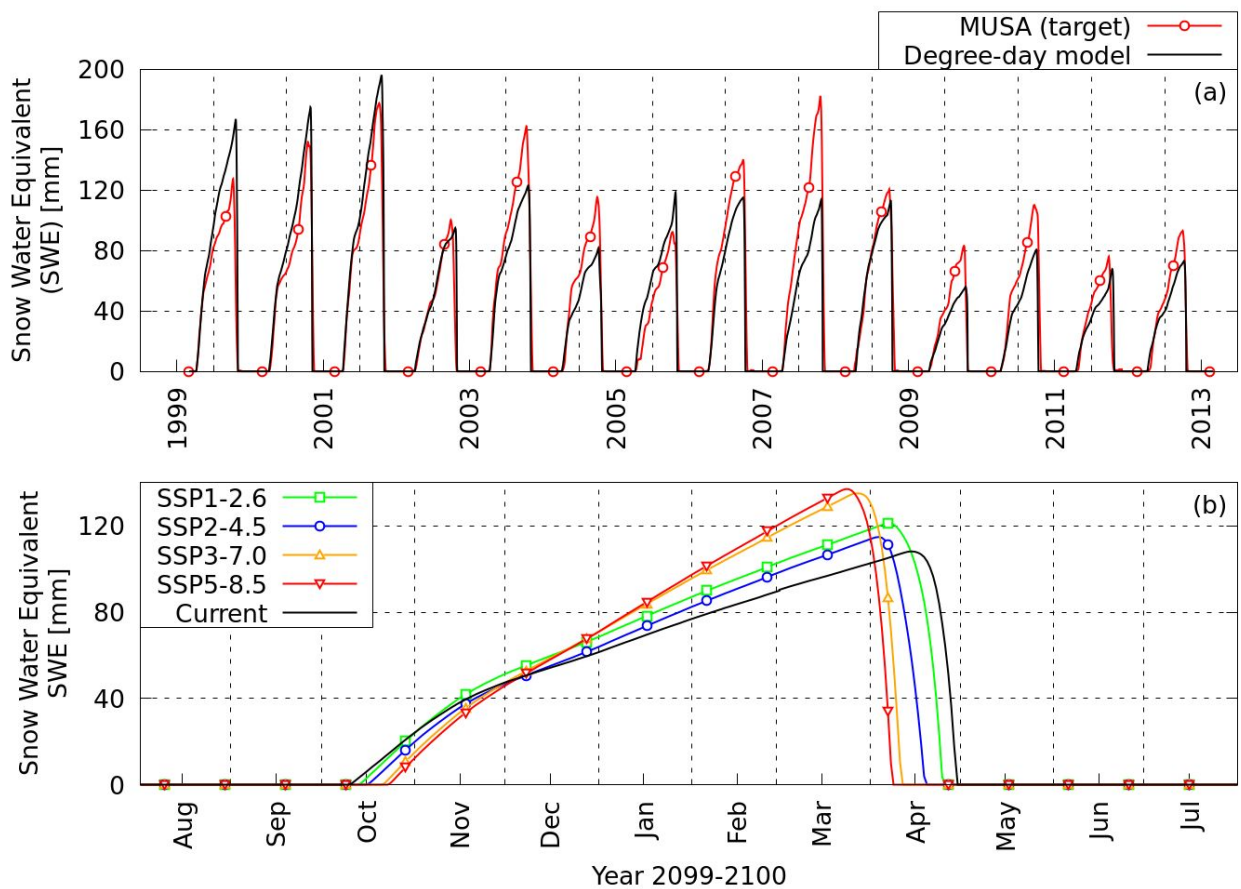
289 From post-processing the computed 2D fields of physical quantities describing the heat and water
290 flow within both the SAS and NAS (two 2.5-km-wide, 10-m-thick slopes), including both frozen
291 and active layers in each slope, a large wealth of data characterising the considered virtual
292 permafrost dynamics is obtained (Supplementary Material C), and below, only the key features of
293 the centennial evolution under climate change are presented.

294

295 **3.1 Soil surface temperature projections**

296 The results of the temperature index approach used for modelling the snow cover of the
297 Kulingdakan watershed is presented in Figure 3. The snow water equivalent (SWE) model shows a
298 good agreement with the MuSA reconstructions (Fig. 3a); hence, this model was used to estimate
299 the SWE under future climate projections (Fig. 3b).

300

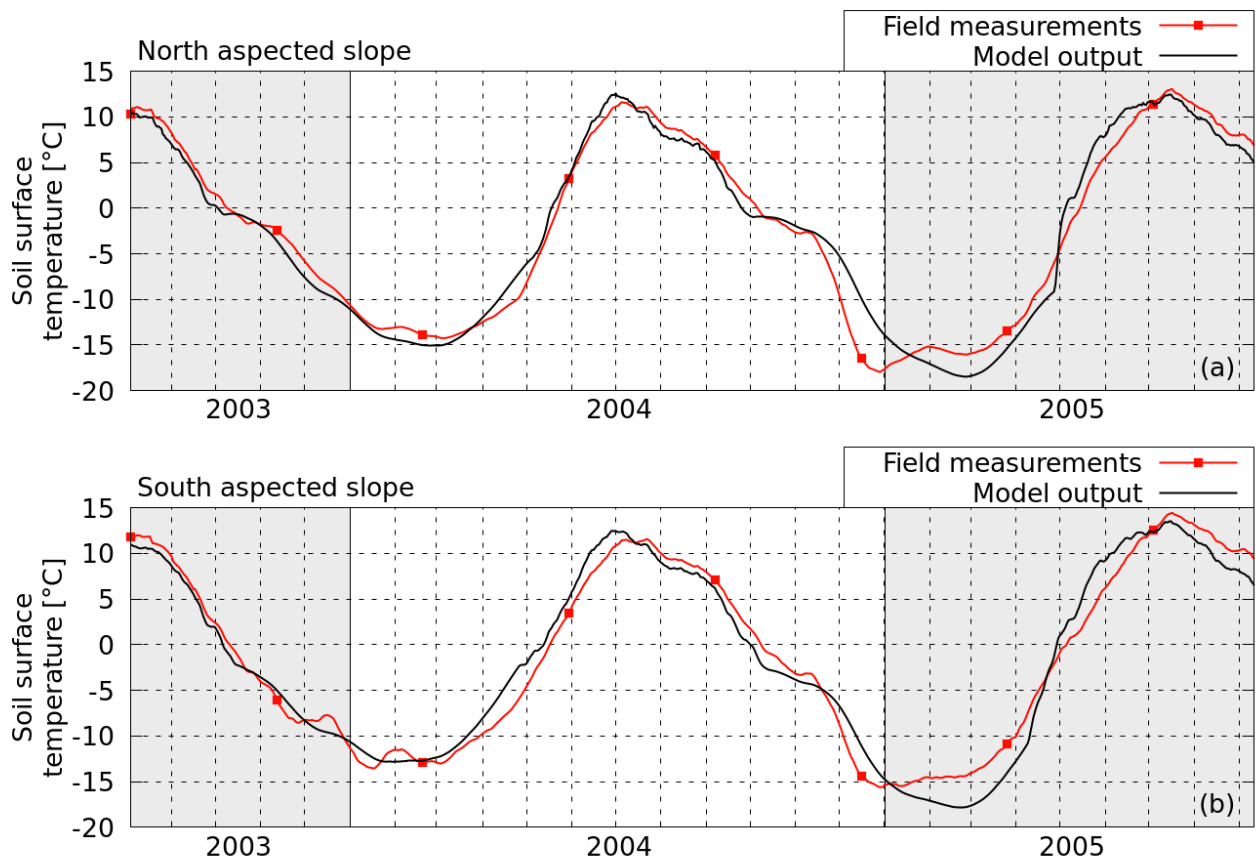


301

302 **Figure 3: (a) Present snow model comparison with MuSA output and (b) projection at the end**
 303 **of the century.**

304 For each slope, the output data of the snow cover model were used as input data for the multiple
 305 regression of the soil surface temperature, along with the air temperature data and precipitation data.
 306 These empirical transfer functions were in good agreement with the observations, as shown in
 307 Figure 4.

308

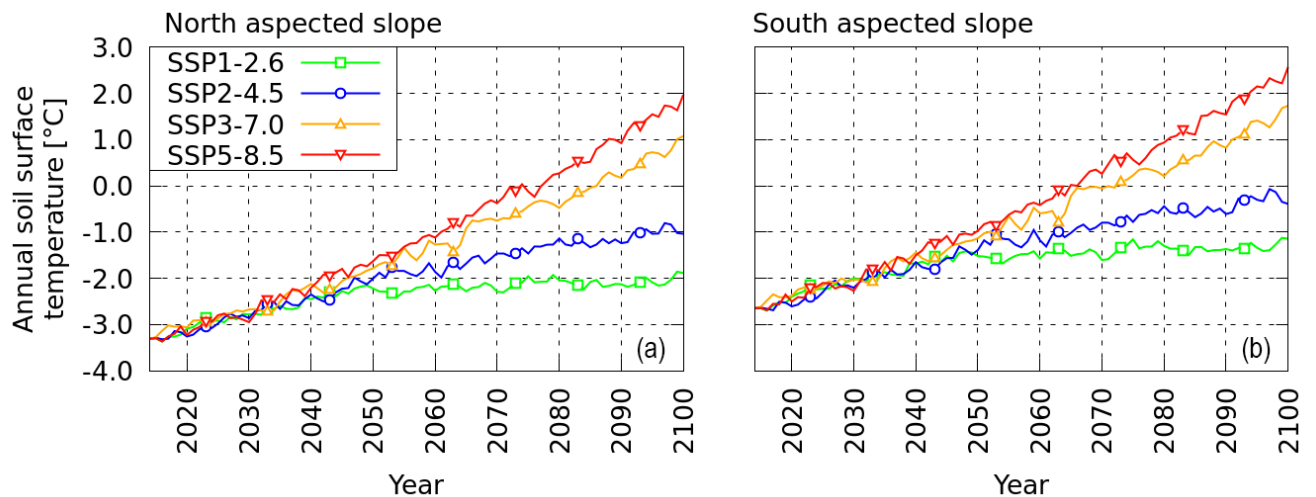


309

310 **Figure 4: Measurements and empirical transfer function estimates for soil surface**
 311 **temperature in present climatic conditions in (a) NAS and (b) SAS.**

312 The L1 norm of the differences between the field measurements and model output is 1.42°C in the
 313 NAS, and 1.56°C in the SAS. The L2 norms of these differences are 0.07°C for both the SAS and
 314 NAS. A more detailed discussion of the behaviour of these empirical transfer functions may be
 315 found in Supplementary Material A.

316 Finally, for each slope, soil temperature projections are obtained for the four considered CMIP6
 317 climate scenarios by applying the developed modelling chain with the projections for air
 318 temperature and precipitation as input data.



319

320 **Figure 5: Soil surface temperature projections over the century based on SSP scenarios**
 321 **obtained using the transfer function described in Supplementary Material A. Transfer**
 322 **function model estimation for soil surface temperature at present conditions for (a) the NAS**
 323 **and (b) SAS of the Kulingdakan watershed(b).**

324

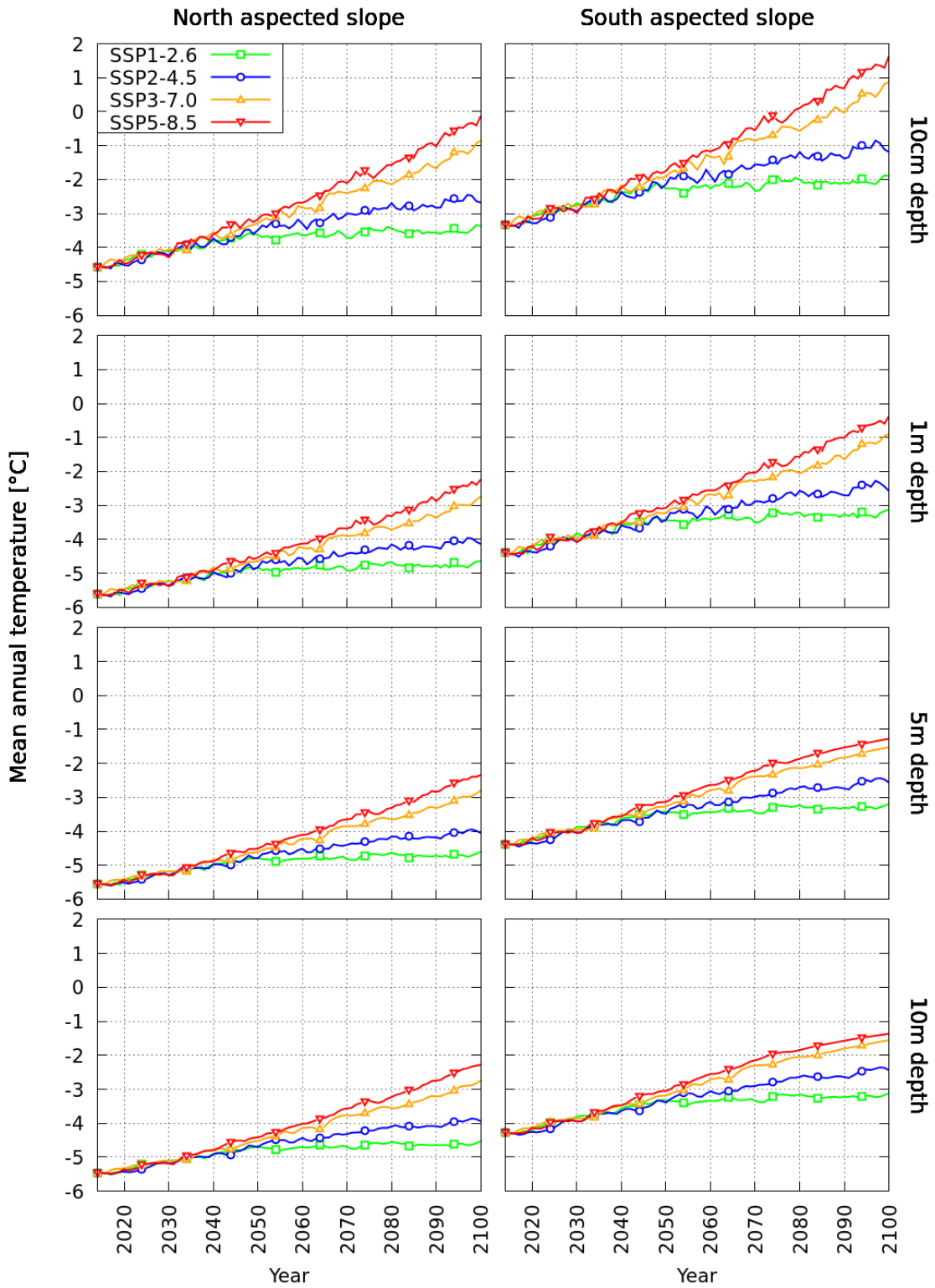
325 The four projections based on the different Shared Socioeconomics Pathways (SSPs) lead to an
 326 increase in the ground surface temperature from +1.4°C (SSP1-2.6) to +5.2°C (SSP5-8.5) between
 327 2014 and 2100 (Fig. 5a and 5b). These rates of increase, roughly equivalent by extrapolation to
 328 +1.7°C/100 years (SSP1-2.6) and +5.9°C/100 years (SSP-8.5), are lower than the projected
 329 increases in air temperature (+1.9°C/100 years for SSP1-2.6 and +7.8°C/100 years for SSP5-8.5)
 330 due to the insulating effect of the snow cover and the vegetation layer, and also due to the thermal
 331 inertia of the soil column below the surface. One can note that for the SSP3-7.0 and SSP5-8.5
 332 scenarios, the mean annual soil surface temperature becomes positive around 2080.

333 **3.2 Trends in soil temperatures**

334 The soil temperature at different depths is one of the key variables for characterising
 335 permafrost dynamics. The multi-annual trends induced by the climate warming of the mean annual
 336 soil temperature between 2014 and 2100 at four depths (10 cm, 1 m, 5 m and 10 m below the
 337 surface) are illustrated in Figure 6.

338

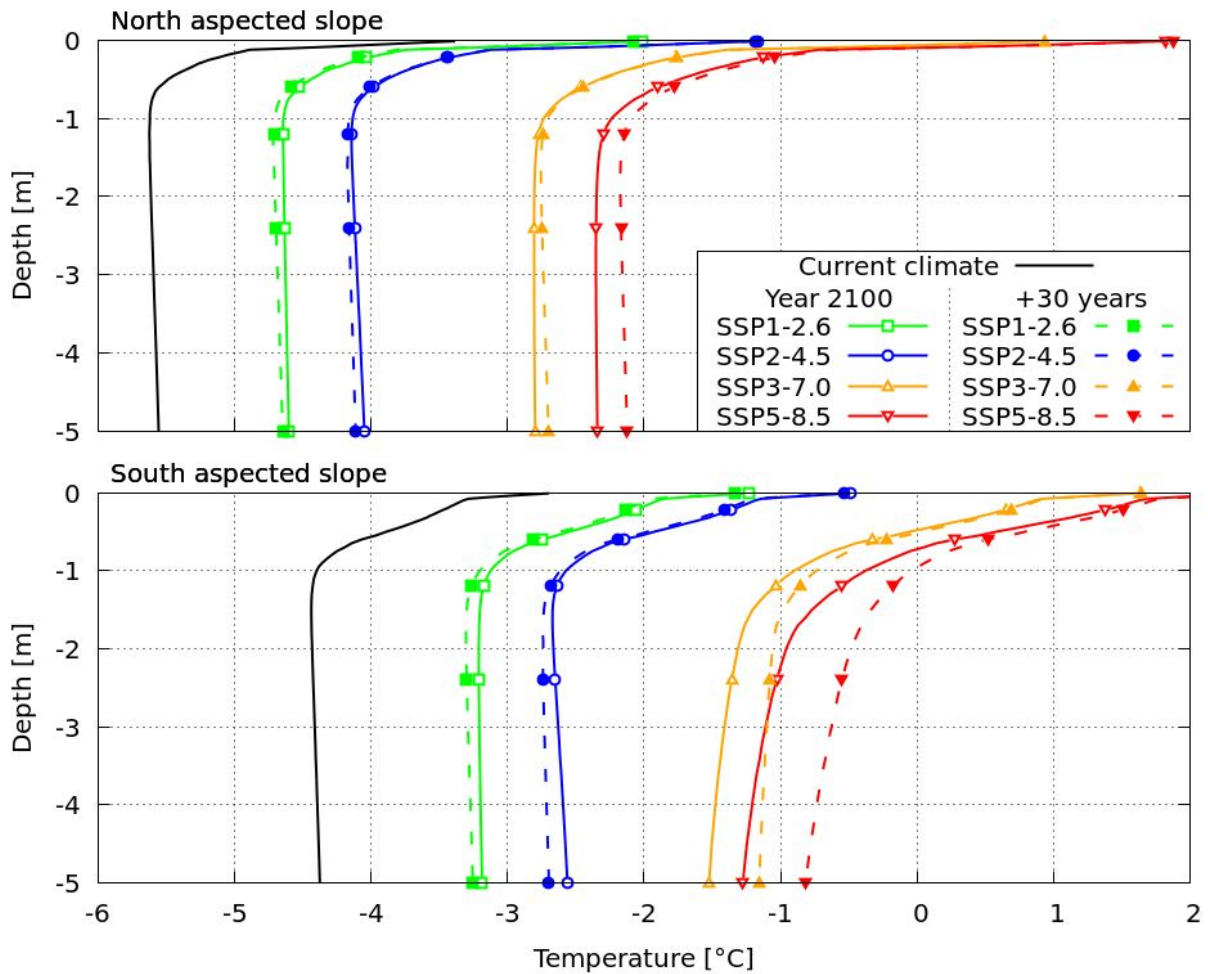
339



340

341 **Figure 6: Mean annual temperature evolution at 10 cm, 1 m, 5 m and 10 m under the surface**
 342 **for each scenario and slope considered.**

343 On both slopes, the soil temperature experiences a significant increase down to 10 m depth,
344 for all climate warming scenarios considered. The annual mean soil temperature even becomes
345 positive close to the surface (10 cm depth) in the SAS for the two high-forcing pathway (hottest)
346 scenarios, by 2080 for SSP5-8.5 and by 2090 for SSP3-7.0. Meanwhile, for the medium scenario
347 SSP2-4.5 and for the low-forcing sustainable pathway (coldest) scenario SSP1-2.6, the mean annual
348 soil temperature stays negative everywhere until 2100. The warming is more intensive in the SAS
349 than in the NAS, and, as expected, the amplitude of soil warming decreases with depth. In the SAS,
350 at 10 cm depth the temperature rise between current conditions and the year 2100 is 1.4 °C for the
351 SSP1-2.6 scenario and 5.0 °C for the SSP5-8.5 scenario, while at 5 m depth, the temperature rises
352 are 1.2°C and 3.1°C, respectively. In the NAS, at 10 cm depth the temperature rise between current
353 conditions and the year 2100 is 1.2°C for the SSP1-2.6 scenario and 4.4°C for the SSP5-8.5
354 scenario, while at 5 m depth, the temperature rises are 1.0°C and 3.2°C, respectively. It should be
355 noted that, for both slopes, the vertical gradient of the temperature in 2100 is higher in scenario
356 SSP5-8.5 than in scenario SSP1-2.6. This indicates a stronger thermal non-equilibrium under more
357 intense warming. For instance, the difference in temperature in 2100 between 10 cm depth and 5 m
358 depth is 3.0°C in the SAS and 2.2 °C in the NAS for scenario SSP5-8.5, while it is 1.3°C in the SAS
359 and 1.2°C in the NAS for the SSP1-2.6 scenario. In order to provide insight into the thermal
360 equilibrium state of the soil columns in each slope in 2100, additional simulations have been
361 performed by applying the projected climatic conditions of the end of the century (averaged over
362 2096–2100) for 30 more years. For each scenario, the vertical soil temperature profiles for 2100 and
363 for the numerical experiments with 30 more years of 2096–2100 climatic conditions are plotted in
364 Figure 7.



365

366 **Figure 7: Annual mean temperature profiles in 2100 and after 30 years of additional cycling**
 367 **of the average climatic forcing between 2096 and 2100.**

368

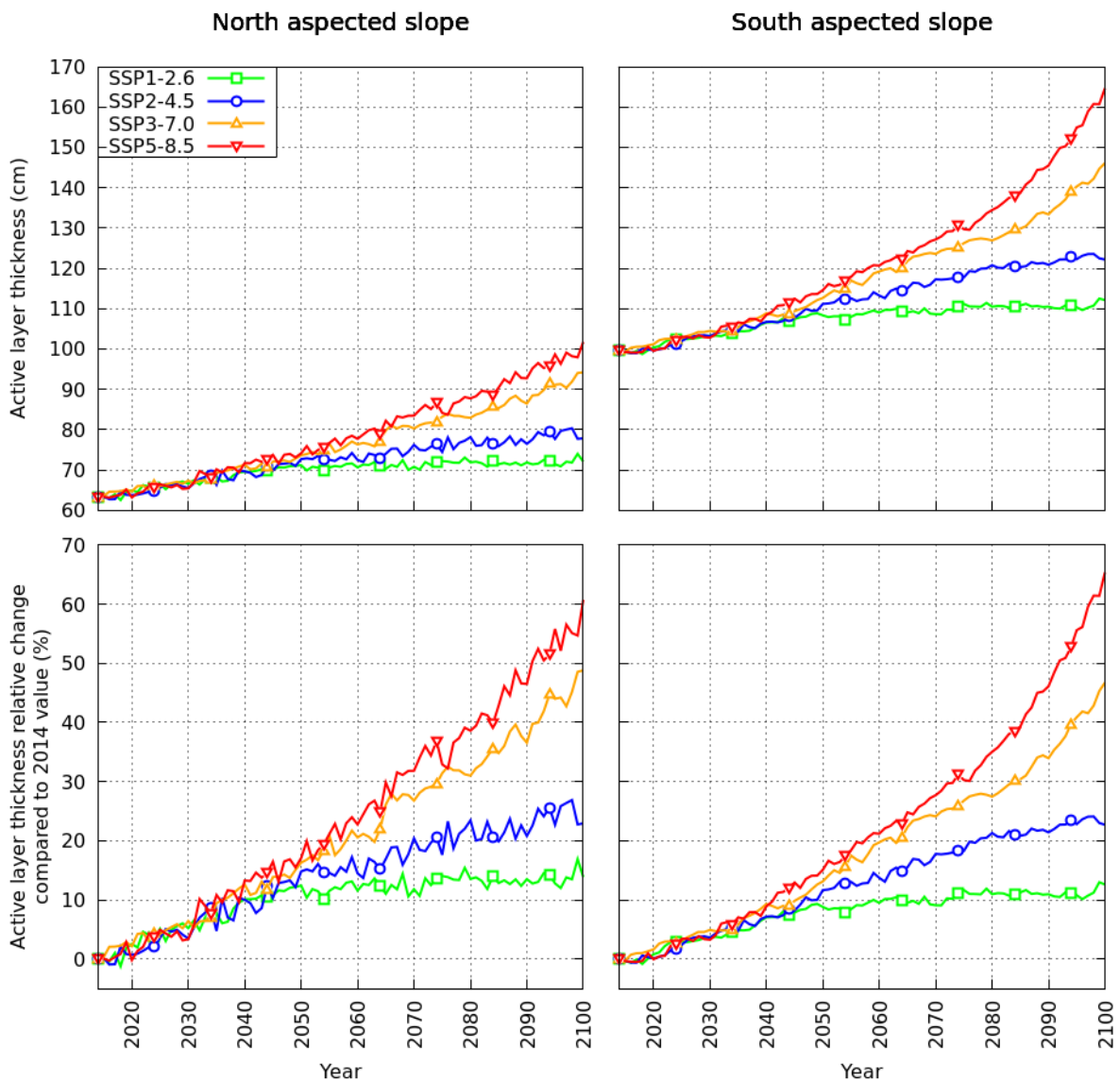
369 Considering the soil temperature profiles in 2100, two regions may be distinguished: the
 370 first metre, with steep positive vertical gradients (the soil surface is warmer than the bottom of the
 371 active layer), and a deeper region, with smoother vertical thermal gradients that are either slightly
 372 negative (SSP1-2.6 and SSP2-4.5 in the NAS and SAS), almost nil (SSP3-7.0 and SSP5-8.5 in the
 373 NAS) or positive (SSP3-7.0 and SSP5-8.5 in the SAS). When comparing these profiles with those
 374 obtained with 30 additional years of modelling in constant ‘2096–2100’ climatic conditions, we
 375 observe important differences in both slopes for scenario SSP5-8.5, and also for scenario SSP3-7.0
 376 and scenario SSP2-4.5, in the SAS.

377

378 **3.3 Active layer thickness evolution**

379 Numerical simulations provide access to the soil temperature at various depths. From the
380 soil temperature profile, the maximum depth with a positive temperature may be computed at each
381 time step. The maximum thawed depth obtained over a year defines the active layer thickness
382 (ALT) of this year. The active layer thickness has been computed for each scenario and each year
383 and is plotted for both the NAS and SAS in Figure 8.

384

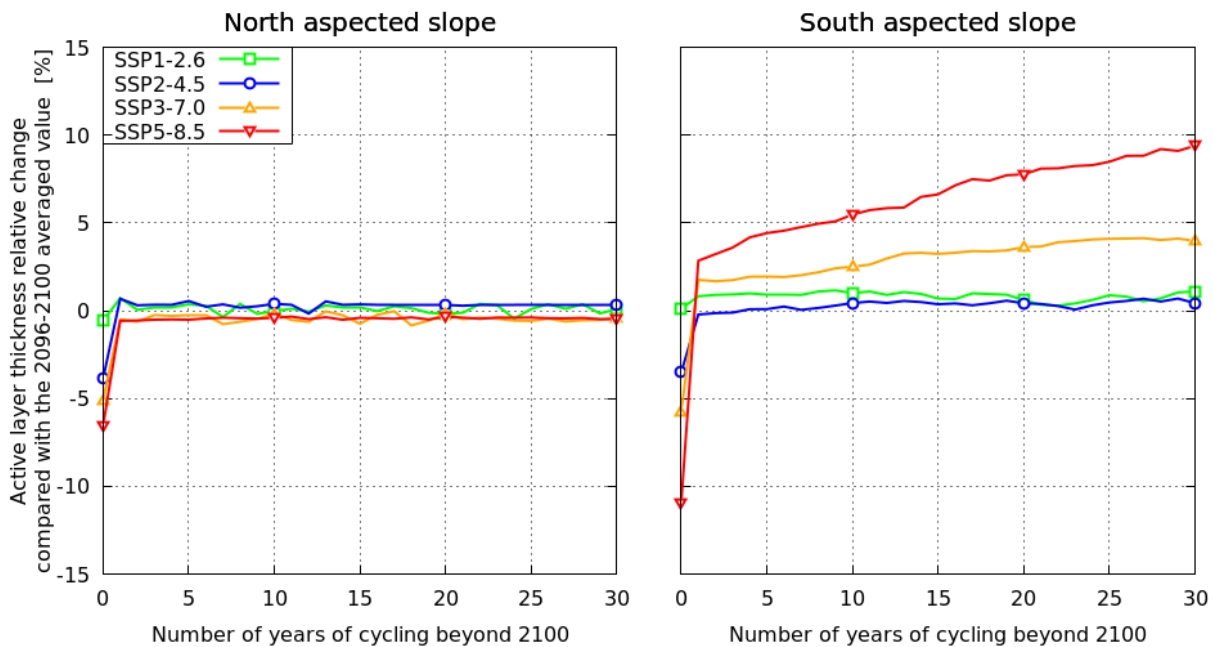


385 **Figure 8: Active layer thickness temporal evolution on the NAS (left) and SAS (right) of the**
386 **Kulingdakan watershed obtained from permaFoam simulations under different SSP**
387 **scenarios. Top : Active layer thickness value. Bottom : Relative change compared to 2014**
388 **value (63 cm for NAS, 100 cm for SAS).**
389

390

391 For both slopes, an increase in the active layer thickness is observed between 2014 and 2100 in
392 every scenario, with a more important thickening in the SAS than in the NAS. SSP1-2.6 leads to an
393 increase of +12.5 cm / +13% for the SAS and +8.8 cm / +14% for the NAS, while SSP5-8.5 leads to
394 a more dramatic increase of +65.1 cm / +65% for the SAS and of +38.5 cm / +61% for the NAS. In
395 the first half of the century, the behaviour of the active layer thickness does not differ significantly
396 between scenarios, with a thickening rate in the ALT of about +3.6 mm/year ($\pm 23\%$) in the SAS
397 and +2.8 mm/year ($\pm 18\%$) in the NAS. However, in the second half of the century (2050–2100),
398 different scenarios lead to very different active layer thickness evolution dynamics. For SSP1-2.6,
399 the thickening rate is rather small, with a rate of +0.60 mm/year for the SAS and +0.32 mm/year for
400 the NAS, while for the SSP5-8.5 scenario, the thickening rate rises to +9.1 mm/year for the SAS
401 and +5.1 mm/year for the NAS. By the end of the simulated period, these thickening rates show no
402 diminishing trend in the SAS, suggesting that the dynamic thermal equilibrium is not reached in the
403 active layer. To illustrate this, Figure 9 shows the active layer thickness evolution for 30 years of
404 additional simulations while keeping the climatic conditions of the end of the century (2096–2100)
405 for each scenario.

406



407

408 **Figure 9: Relative change in active layer thickness compared with the average value for 2096–**
409 **2100 over 30 years of spin-up for a synthetic year obtained by averaging climatic conditions**
410 **between 2096 and 2100.**

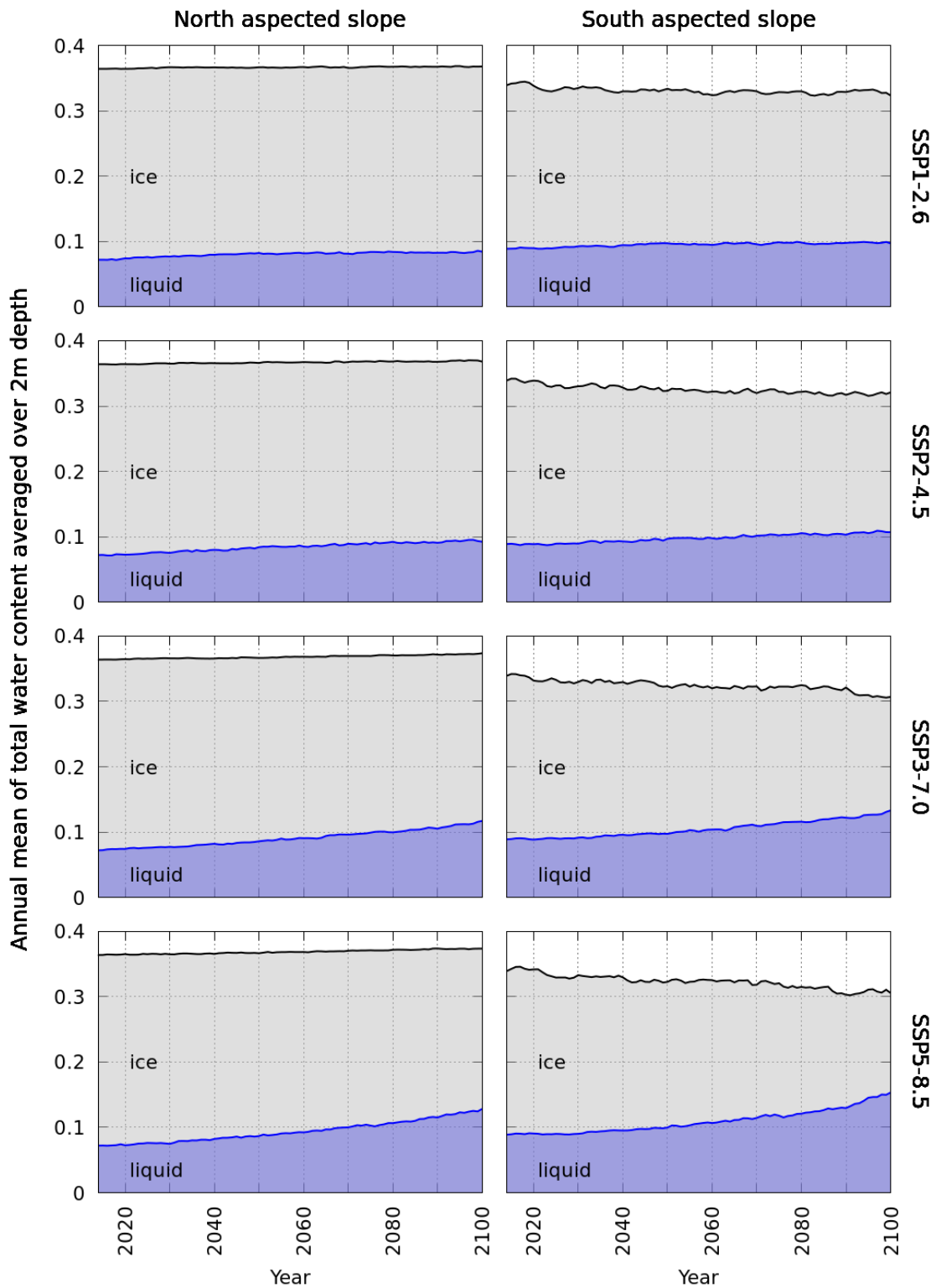
411

412 Overall, the active layer is not far from thermal equilibrium on both slopes for the low-forcing
413 sustainable pathway (SSP1-2.6) and medium (SSP2-4.5) climatic scenarios. However, when
414 considering the high-forcing pathway SSP5-8.5 scenario, an important thermal inertia effect appears
415 in the SAS, with an additional active layer thickness increase over these 30 years of +10.4 %
416 compared to the 2096–2100 value, i.e. an increase of +17 cm. This additional change in the active
417 layer thickness brings the resulting change compared to the 2014 value to +77 cm (+77%) for the
418 SSP5-8.5 scenario for the SAS. The abrupt change observed at the end of the first year of cycling is
419 a direct observation of the abrupt change in climatic forcing (from 2100 forcings to 2096–2100
420 averaged conditions). Interannual variability is included in CMIP6 scenarios, as can be seen in
421 Figure 2 for both the air temperature and precipitations. For the NAS, the active layer is back to
422 equilibrium in a year, which is a sign of a short response time. For the SAS, and particularly for the
423 steepest scenarios, this effect is added to a longer response time change, as discussed previously.

424 **3.4 Trends in soil moisture**

425 The soil moisture content experienced less important changes than the thermal regime under
426 the considered climate change scenario. To illustrate the soil moisture evolution near the surface,
427 the total water, liquid water and ice volumetric contents have been averaged over the first 2 m of the
428 soil for each slopes, and their 2014–2100 evolutions have been plotted in Figure 10 for the four
429 climatic scenarios. Note that the 2 m surface soil layer thickness considered for this quantification
430 encompasses the entire area with water content evolution under the climate change scenarios.
431 Regardless of the scenario, there is no significant evolution of the total water content in the first 2 m
432 of soil in the NAS, and the only noticeable change is the increase in the proportion of liquid water
433 (+17% in SSP1-2.6, +28 % in SSP2-4.5, +62% in SSP3-7.0, +78% in SSP5-8.5), suggesting an
434 increase in the amount of liquid water available for vegetation. In the SAS, however, the first 2 m of
435 the soil exhibited a slight but detectable diminishing of the total water content by 2100 (-5 % in
436 SSP1-2.6 and SSP2-4.5, -10% in SSP3-7.0 and SSP5-8.5). On the other hand, the proportion of
437 liquid water over ice increases (+9% in SSP1-2.6, +20% in SSP2-4.5, +50% in SSP3-7.0, +72% in
438 SSP5-8.5). Therefore, on the SAS, climate warming may result in an increase in the amount of
439 liquid water available for vegetation. This finding is important for heat and water transfers in the
440 soil, given the strong couplings and non-linearities between these transfers. For instance, decreasing
441 the total water content induces a decrease in the soil thermal inertia, while decreasing the share of
442 ice versus liquid water induces a decrease in the apparent thermal conductivity. This can also

443 impact the vegetation dynamics, since vegetation takes up only liquid soil water for transpiration. It
444 should be emphasised that the presented partitioning between liquid water and ice is based on the
445 mean annual quantities. This provides a considerably smaller proportion of liquid water compared
446 to that at the end of the active season (second half of September), when the active layer is at its
447 maximum thickness.

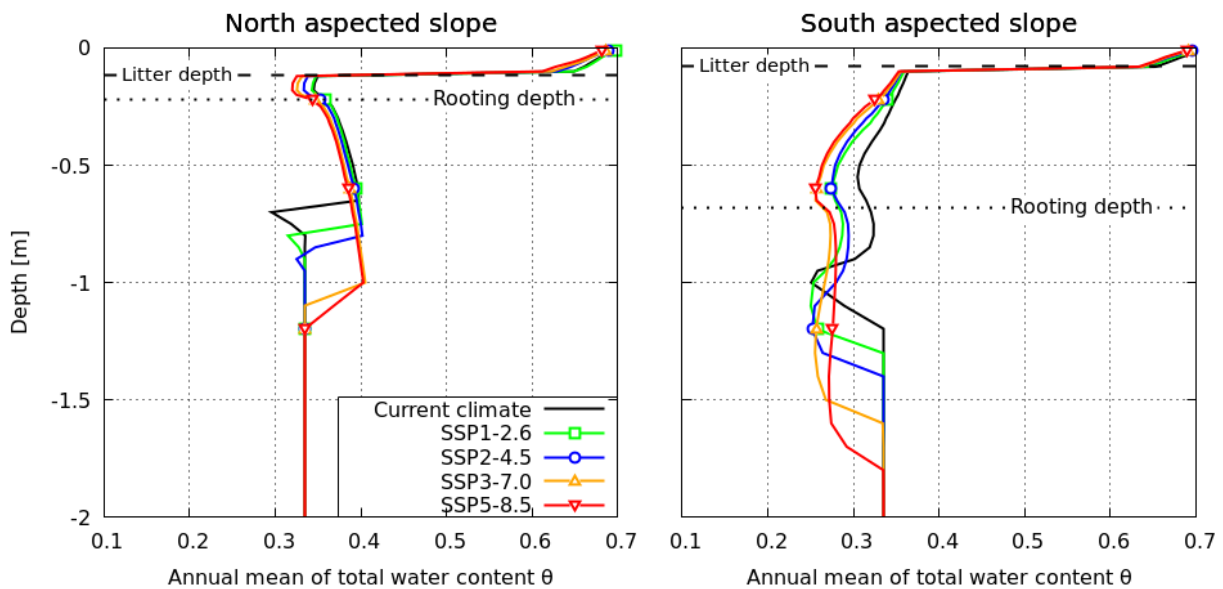


448

449 **Figure 10: Annual mean of total water content [m³ of water / m³ of soil], liquid water content**
 450 **and ice content averaged over 2m depth in different climate projections.**

451

452 In order to investigate the local variation of the moisture content in the rooting zone and in
 453 the active layer of each slope, the vertical profiles of the mean annual total water content have been
 454 plotted in Figure 11 for current climatic conditions and for the year 2100 under the SSP1-2.6, SSP2-
 455 4.5, SSP3-7.0 and SSP5-8.5 scenarios. The processes driving the evolution of vertical moisture
 456 profiles are complex; they involve coupled and non-linear heat and water transfers, as well as
 457 changing evapotranspiration fluxes. The relevant changes in the vertical moisture profiles can be
 458 described as follows. The water profiles do not change significantly in the highly porous organic
 459 horizon for both slopes. In the mineral horizon, the behaviours of the SAS and NAS contrast more
 460 due to downward vertical moisture gradients (and thus, according to the generalised Darcy's law,
 461 upward water movements) in the NAS and upward vertical moisture gradients (and thus downward
 462 water movements) in the SAS. In the NAS, the only evolution with climate change is a thickening
 463 of the zone with a downward vertical moisture gradient (i.e. an upward water flux) alongside the
 464 thickening of the active layer, with no significant changes in the gradient itself. Meanwhile, in the
 465 SAS, along with the thickening of the zone with water movements (i.e. moisture gradients) that
 466 comes with active layer thickening, significant changes in the upward moisture gradients are
 467 expected to occur: the hotter the scenario, the steeper the gradients, and thus the stronger the
 468 downward water fluxes.



469
 470 **Figure 11: Two-metre depth profiles of the annual mean of the total water content [m³ of**
 471 **water / m³ of soil] in 2100: projections compared to current state.**

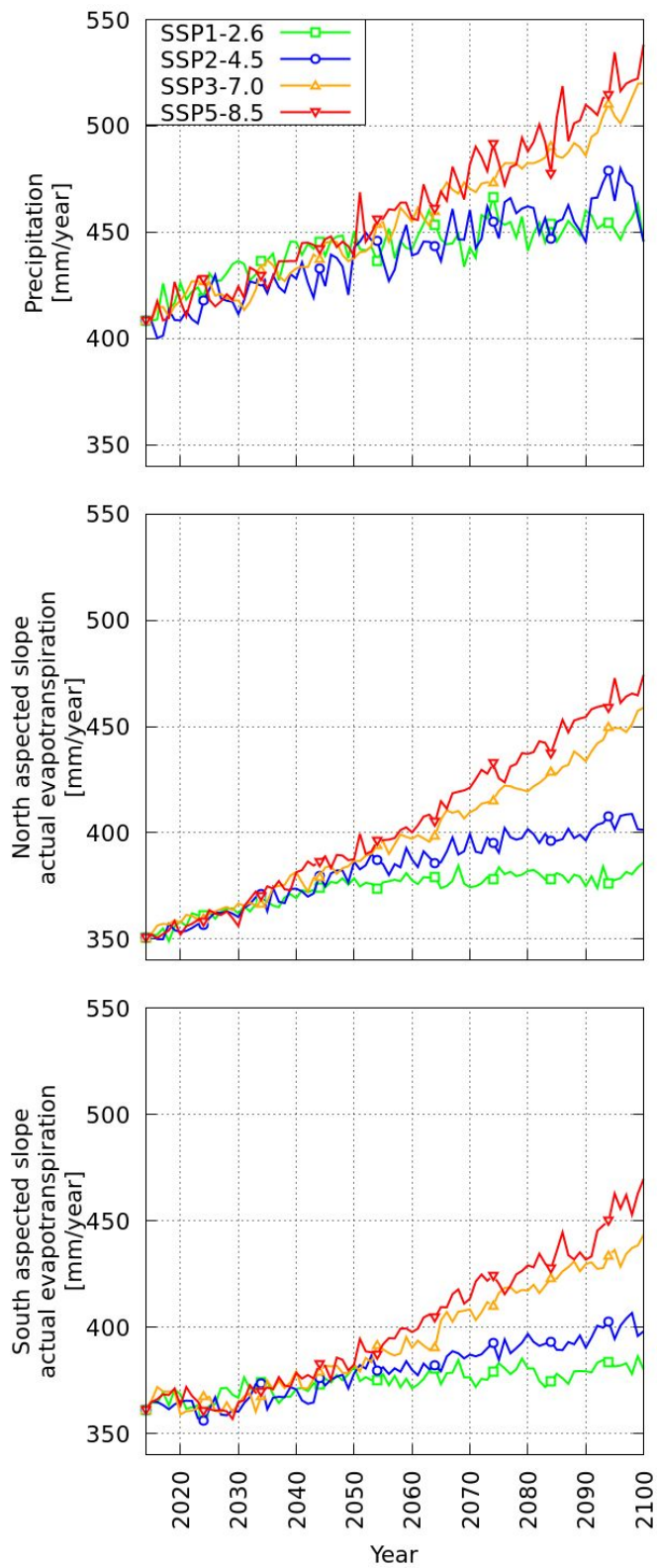
472

473 **3.5 Water fluxes**

474 The water fluxes also significantly change with climate change on both slopes for every
475 scenario. Evapotranspiration is the most important component of the hydrological budget in
476 Kulingdakan. Focusing on this dominant component, Figure 12 presents the centennial evolution of
477 evapotranspiration on both slopes and precipitation for the four climate change scenarios. A
478 significant increase in evapotranspiration is simulated in all cases, with an increase between +19
479 mm / +5% (SSP1-2.6) and +108 mm / +30% (SSP5-8.5) in the SAS, and between +35mm / +10%
480 and +123 mm / +35% in the NAS. The increase in the evapotranspiration fluxes in Kulingdakan is
481 correlated to the increase in precipitation, with similar rates for both slopes.

482

483



484

485 **Figure 12: Precipitation and actual evapotranspiration evolution over the century**

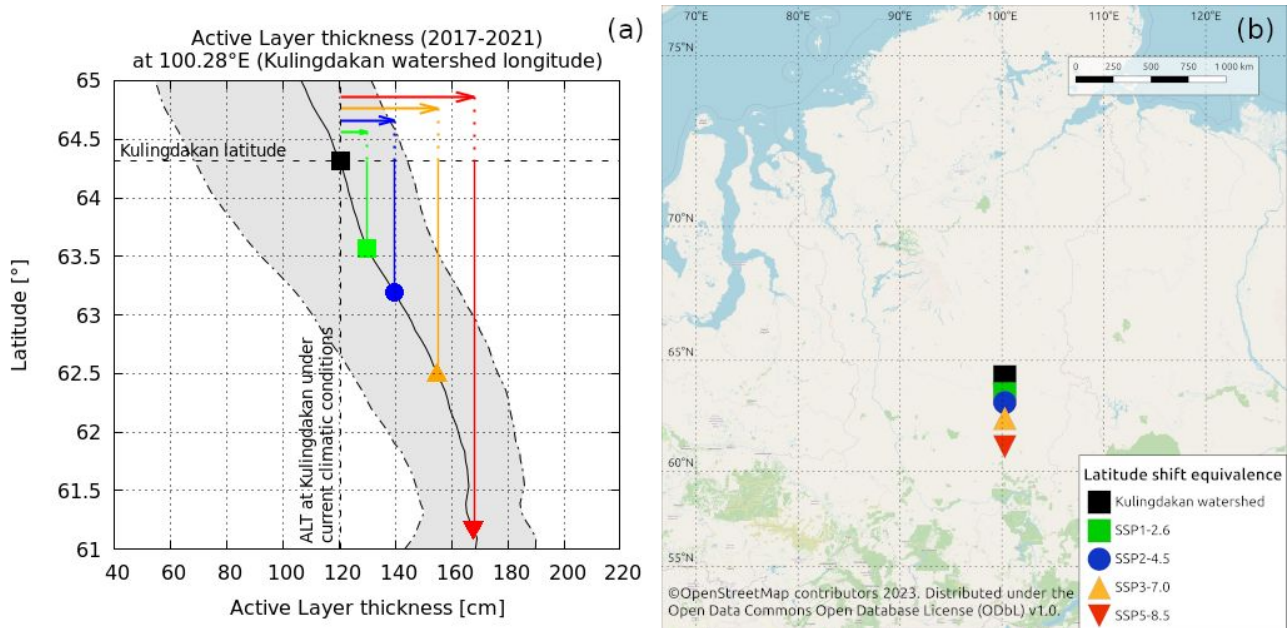
486 Similar to previous simulations of Mean Annual Temperature, soil surface temperature and Active
487 Layer Thickness, the evolution is globally similar among scenarios until 2050, with significant
488 divergences appearing only between 2050 and 2100.

489 **4 Discussion**

490 The numerical results obtained by the mechanistic modelling of heat and water transfer
491 within the permafrost and active layer of Kulingdakan document the physical response to be
492 expected within this catchment under climate change, with soil warming (Fig. 6) and active layer
493 thickening (Fig. 8) in all climate scenarios. An important spatial variability of this thermal response
494 is identified, in relation with the aspect of the slopes, which stems from a sizable contrast in the
495 vegetation cover, hydrologic and thermal state and active layer dynamics, as currently observed
496 between the two slopes of the catchment (Prokushkin et al, 2007). Indeed, since the NAS is wetter,
497 its thermal inertia is more important due to the larger amount of latent heat that must be provided in
498 order to thaw and warm its soils, compared to the drier soils of the SAS. This difference in moisture
499 content is largely due to differences in the tree cover biomass and physiology. In particular, the
500 deeper root layer in the SAS compared to the NAS induces more intensive evapotranspiration,
501 under both current (Orgogozo et al., 2019) and future climate conditions. Note that this contrast
502 between the two slopes tends to diminish with climate warming (Fig. 12), although the SAS will
503 always remain drier than the NAS (Fig. 10). The pattern of water fluxes within the active layer, with
504 an upward flux to the thinner, close-to-the-surface root layer in the NAS and a downward flux
505 toward the bottom of the thicker root layer in the SAS is also preserved under climate change, with
506 an intensification of the fluxes in the SAS under the high-forcing pathway scenarios (Fig. 11).
507 Furthermore, the thicker moss layer in the NAS is likely to alleviate more efficiently the effect of
508 changes in the climatic conditions on soil compared to that in the SAS. Because our modelling takes
509 into account the root water uptake mechanistically (Orgogozo et al., 2023) and the low vegetation
510 insulating effect empirically (Supplementary Material A), the warming of the soil and the
511 thickening of the active layer under climate change are significantly more pronounced in the SAS
512 than in the NAS. This spatial variability in permafrost dynamics of forest environments, persistent
513 at all climate change scenarios, reflects the prominent role of micro-climatic conditions in the
514 responses to climate change that has been demonstrated recently in the literature (Zellweger et al.,
515 2020). It must be emphasised that all the numerical results of this study have been obtained
516 considering the vegetation in its present state. The strong local variabilities of the vegetation cover
517 depending on the permafrost conditions in the Kulingdakan catchment (Orgogozo et al., 2019) and,
518 from a broader perspective, in the Arctic (Oehri et al., 2022), are consistent with the tight
519 connections between the evolution of vegetation under climate change (e.g. Vitasse et al. 2009,

2011; Rew et al., 2020) and the permafrost pattern, which has not been explicitly considered in this study. At the centennial time scale, changes in the tree growth rate, the forest fire frequency or the nature of the vegetation cover may exert important impacts on permafrost conditions (Cable et al., 2016; Fedorov et al., 2019; Rew et al., 2020; Li et al., 2021; Heijmans et al., 2022). Meanwhile, without belittling these complex interactions between vegetation and permafrost dynamics, this study shows that important impacts of climate change on the permafrost dynamics of the forested continuous permafrost area are to be expected, even with the steady state of the vegetation. We noted that the more intense the climate change, the more pronounced these thermal responses. For instance, under the SSP5-8.5 scenario, a maximum evolution of the active layer thickness is +65 cm / +65% for the SAS and +39 cm / +61% for the NAS, while in the SSP2-4.5 scenario, an increase of +23 cm / +23% for the SAS and of +15 cm / +23% for the NAS is anticipated. Using empirical transfer functions to approximate the soil surface temperature from atmospheric conditions under climate change poses the problem of extrapolation, for instance under extreme hot weather conditions that may occur in the future, which are unprecedented in the training period 1999–2014. However, performing the mechanistic modelling of the surface energy balance in extreme weather conditions under permafrost contexts was beyond the scope of this work. Additionally, it must be noted that for now in permaFoam, evapotranspiration is assumed to be solely constituted by transpiration, while the evaporation within the soil is neglected (Orgogozo et al., 2019). This assumption is made in the context of the study of boreal forest areas, in which transpiration largely dominates over evaporation in the hydrological budget (e.g. Park et al., 2021). Meanwhile, evaporation may dominate in tundra environments (Clark et al., 2023) and likely to increase in the future in forested environments. Since soil evaporation adds another coupling between heat and water transfers through exchanges of latent heat, it could directly affect the soil temperature evolution. These points should constitute a scope of future modelling works.

To produce a broader geographical context of the active layer thickening projections simulated at the scale of a small catchment, a comparison of centennial evolutions under climate change with large geographical coverage is performed using a substituting space for time approach (Fig. 13).



548

549 **Figure 13: (a) Equivalence between simulated active layer thickening by 2096–2100 under**
 550 **climate change (SAS and NAS average) and southward latitudinal shift in current climatic**
 551 **conditions (2017–2021). – Latitudinal trend (black line – average over a 1°lat. × 1°long.**
 552 **polygon) and envelope (in grey – min./max. over years within the same polygon) extracted**
 553 **from Permafrost CCI (Westermann et al., 2024). (b) Representation of the latitudinal**
 554 **southward shift equivalent to each climate scenario’s active layer thickening on the regional**
 555 **map.**

556

557 The simulated thickening of the active layer, averaged over both slopes of Kulingdakan, is depicted
 558 as southward latitudinal shifts along the meridian passing by Kulingdakan, i.e. with a north-south
 559 translation along 100.28 °E (Fig. 13). The latitudinal evolution of the active layer thickness along
 560 the current meridian is computed based on the permafrost_CCI dataset (Westermann et al., 2024)
 561 by averaging the value of the multi-annual mean of the active layer thickness for the 2017–2021
 562 period over a polygon of 1° of latitude by 1° of longitude centred on the considered meridian and
 563 browsing the latitude between 67°N and 57°N. The 1°-1° polygon was considered big enough to
 564 smooth the small-scale non-homogeneities (at km scale) and small enough to capture the latitudinal
 565 effect, including biome transitions (~hundreds of km, e.g. Anisimov et al., 2015) In Figure 13a, the
 566 black line describes the multi-annual (1997–2019) temporal average of the spatial average of the
 567 active layer thickness over a 1°-1° polygon centred on a moving latitude ; the grey shaded area
 568 represents the minimum/maximum obtained for this spatial average during the considered period. It
 569 can be seen that, in the high-forcing pathway scenario SSP5-8.5, the active layer thickening would

570 correspond to a 349 km southward shift, while in the medium scenario SSP2-4.5, it would
571 correspond to a 124 km southward shift.

572 Under a permanently changing climatic context, an important question is the state of thermal
573 equilibrium versus non-equilibrium of the permafrost (Obu et al., 2019): is the climate change
574 induced warming slow enough that permafrost may be considered at every time close to the thermal
575 equilibrium with climatic conditions, or on the contrary, do the transient effects dominate the
576 thermal dynamics of permafrost under climate change? The simulation results of this work provide
577 information for characterising the degree of thermal equilibrium of the continuous permafrost, in a
578 forested study site under various scenarios of climate change. First of all, we emphasise that, since
579 the bottom thermal boundary condition in our modelling is the geothermal heat flux (Duchkov et
580 al., 1997), the assumption of overall thermal equilibrium at depth (<10 m) in the hundreds of metres
581 of the thick permafrost of the Putorana plateau (Pokrovsky et al., 2005) is implicitly made.
582 Meanwhile, the temperature profiles shown in Figure 7 demonstrate that under this assumption the
583 thermal equilibrium state of the first 10 m of soil in 2100 depends on both the climate change
584 scenario and the slope aspect. In the NAS, the thermal equilibrium of the first 10 m of soil is
585 achieved by 2100 in every climate scenario, with only a slight shift between the 2100 and
586 (2100+30) conditions in the SSP5-8.5 scenario. Additionally, with sub-zero vertical thermal
587 gradients in each scenario, only small heat exchanges between the surface and the deep layer may
588 occur. On the contrary, by 2100 in the SAS, strong thermal non-equilibrium is encountered in the
589 two high-forcing pathway scenarios, SSP3-7.0 and SSP5-8.5 (Fig. 7 and 8). Under these scenarios,
590 sizable evolutions of temperature profiles are expected between 2100 and 2100+30. Moreover, for
591 these two scenarios, the vertical thermal gradients between 1 and 10 m depth are clearly positive
592 (considering an upward vertical axis), which implies an ongoing heat flux from the surface to the
593 depths. In this case, the permafrost is warming below 10 m, at a rate that we implicitly assume to be
594 small enough that it does not modify the total amount of heat stored within this deep permafrost. As
595 such, in scenarios SSP3-7.0 and SSP5-8.5, the climate change clearly induces the transient warming
596 of the permafrost below 10 m depth in the SAS of the Kulingdakan watershed. One could note
597 slightly decreasing trends in the soil temperature under scenarios SSP1-2.6 and SSP2-4.5. This is
598 due to inter-annual variabilities in both the precipitation and air temperature in CMIP6 projections
599 (Fig. 2). Therefore, the year 2100 may offer different conditions from those observed in the 2096-
600 2100 average, which is repeated over 30 cycles to assess the equilibrium state of the permafrost.,
601 For example, in SSP2-4.5, the last decade experiences an important annual precipitation peak, up to

602 475 mm/year, centred around 2095, before a decreasing trend in the second part of the decade,
603 ending up with a precipitation of 410 mm/year projected in 2100. This results, for the year 2100, in
604 a decrease in the snow cover insulating effect in winter and thus a lowering of the soil surface
605 temperature (Fig. 5), compared to the conditions encountered in the previous decade.

606 Overall, the results of the present study may be used to improve our understanding of the
607 climate-warming-related changes in the wide areas of boreal forest on continuous permafrost, with
608 implications for continental surfaces (Revich et al., 2022), ecosystems (Wang and Liu 2022) and
609 element cycles (Schuur et al., 2022), and related global consequences and feedbacks. Mechanistic
610 modelling, although it is computationally costly, is capable of providing quantitative information
611 for these research fields. This approach should be applied in other environmentally monitored
612 boreal watershed, in order to numerically characterise the physical response of permafrost to
613 climate change under various environmental contexts, for instance, in Northern Sweden (Auda et
614 al., 2023) and Western Siberia (Cazaurang et al., 2023).

615 **5 Conclusion**

616 Four main conclusions that could be drawn from this numerical study are the following:

- 617 - All climate change scenarios trigger significant soil warming (+1.8°C in the SAS and +1.5°C in
618 the NAS under the SSP2-4.5 scenario at 1 m depth according to the presented simulations) and an
619 increase in the active layer thickness (+23 cm / +23% in the SAS and +15 cm / +23% in the NAS
620 under the SSP2-4.5 scenario) for both slopes of the Kulingdakan watershed. The projected increase
621 in the active layer thickness under the SSP2-4.5 scenario would be equivalent to a ~120 km
622 southward shift in current climatic conditions, and to a ~350 km southward shift under the SSP5-8.5
623 scenario.
- 624 - For all climate change scenarios, the combination of soil warming and an increase in precipitation
625 leads to an important increase in evapotranspiration for both slopes (+37 mm / +10% in the SAS
626 and +51 mm / +14% in the NAS under the SSP2-4.5 scenario). Meanwhile, the mean annual soil
627 moisture decreases only slightly in the NAS (-2.3% under the SSP2-4.5 scenario, averaged over the
628 22 cm of rooting depth), but the decrease is more pronounced in the SAS (-6.0% under the SSP2-
629 4.5 scenario, averaged over the 68 cm of rooting depth).
- 630 - The important spatial variability observed in the Kulingdakan watershed illustrate the key role of
631 meso-climatic conditions and small-scale geomorphological contrasts in the permafrost response to
632 climate warming

633 - Under the two high-forcing pathway scenarios of climate change, SSP3-7.0 and SSP5-8.5, the
634 near-surface permafrost of the SAS of the Kulingdakan watershed is in a non-equilibrium thermal
635 state in 2100, and further investigation is needed to assess whether or not the permafrost below 10
636 m depth will be close to thermal equilibrium in this region. This indicates the need to develop non-
637 equilibrium modelling approaches for regional and global permafrost modelling under climate
638 change.

639 The approach developed in this study can be applied to other high-latitude permafrost-affected
640 catchments, provided that the necessary information on current thermal and hydrological parameters
641 of the soil as well as vegetation coverage, is available.

642

643 **Competing interests**

644 The corresponding author has declared that none of the authors has any competing interests.

645 **Acknowledgments**

646 This work has been funded by the French National Research Agency ANR (grant no ANR-19
647 CE46-0003-01) and benefited from access to the supercomputers of CALMIP (project p12166) and
648 GENCI (project A0140410794, TGCC). This work was supported by a French government grant
649 managed by the Agence Nationale de la Recherche under the ‘Investissements d’avenir’ program
650 (reference ‘ANR-21-ESRE-0051’). Oleg Pokrovsky is grateful for partial support from the TSU
651 Development Programme PRIORITY – 2030 and project PEACE of PEPR FairCarboN ANR-22-
652 PEXF-0011. Anatoly Prokushkin is supported by State Assignment no. 0287-2021-0008. Esteban
653 Alonso Gonzalez is supported by the European Space Agency through the Climate Change
654 Initiative postdoctoral grant.

655 **References**

656 Alonso-González, E., Aalstad, K., Baba, M. W., Revuelto, J., López-Moreno, J. I., Fiddes, J.,
657 Essery, R., and Gascoin, S.: The Multiple Snow Data Assimilation System (MuSA v1.0), *Geosci.*
658 *Model Dev.*, 15, 9127–9155, <https://doi.org/10.5194/gmd-15-9127-2022>, 2022.

659

660 Anisimov, O. A., Zhiltcova, Y. L., and Razzhivin, V. Y.: Predictive modeling of plant productivity
661 in the Russian Arctic using satellite data, *Izvestiya Atmospheric and Oceanic Physics*, 51(9), 1051–
662 1059, <https://doi.org/10.1134/S0001433815090042>, 2015.

663

664 Arndal, M. F., and Topp-Jørgensen, E. (Eds.): *INTERACT Station Catalogue – 2020*, DCE –
665 Danish Centre for Environment and Energy, Aarhus University, Denmark, 190 pp., ISBN 978-87-
666 93129-15-3, www.eu-interact.org, 2020.

667

668 Auda, Y., Lundin, E. J., Gustafsson, J., Pokrovsky, O. S., Cazaurang, S., and Orgogozo, L.: A new
669 land cover map of two watersheds under long-term environmental monitoring in the Swedish Arctic
670 using Sentinel-2 data, *Water*, 15, 3311, <https://doi.org/10.3390/w15183311>, 2023.

671

672 Bartsch, A., Pointner, G., Nitze, I., Efimova, A., Jakober, D., Ley, S., Högström, E., Grosse, G., and
673 Schweitzer, P.: Expanding infrastructure and growing anthropogenic impacts along Arctic coasts,
674 *Environ. Res. Lett.*, 16, 115013, <https://doi.org/10.1088/1748-9326/ac3176>, 2021.

675

676 Blok, D., Heijmans, M. M. P. D., Schaepman-Strub, G., Van Ruijven, F., Parmentier, F. J. W., and
677 Maximov, T. C.: The cooling capacity of mosses: Controls on water and energy fluxes in a Siberian
678 tundra site, *Ecosystems*, 14, 1055–1065, <https://doi.org/10.1007/s10021-011-9463-5>, 2011.

679

680 Braithwaite, R. J., and Olesen, O. B.: Calculation of glacier ablation from air temperature, West
681 Greenland, in: *Glacier Fluctuations and Climatic Change*, edited by: Oerlemans, J., Kluwer
682 Academic Publishers, 219–233, 1989.

683

684 Biskaborn, B. K., Smith, S. L., Noetzli, J., *et al.*: Permafrost is warming at a global scale, *Nat.*
685 *Commun.*, 10, 264, <https://doi.org/10.1038/s41467-018-08240-4>, 2019.

686

687 Cable, W. L., Romanovsky, V. E., and Jorgenson, M. T.: Scaling-up permafrost thermal
688 measurements in western Alaska using an ecotype approach, *The Cryosphere*, 10, 2517–2532,
689 <https://doi.org/10.5194/tc-10-2517-2016>, 2016.

690

691 Cazaurang, S., Marcoux, M., Pokrovsky, O. S., Loiko, S. V., Lim, A. G., Audry, S., Shirokova, L.
692 S., and Orgogozo, L.: Numerical assessment of morphological and hydraulic properties of moss,
693 lichen and peat from a permafrost peatland, *Hydrol. Earth Syst. Sci.*, 27, 431–451,
694 <https://doi.org/10.5194/hess-27-431-2023>, 2023.
695

696 Clark, J. A., Tape, K. D., and Young-Robertson, J. M., Quantifying evapotranspiration from
697 dominant Arctic vegetation types using lysimeters, *Ecohydrology*, 16(1), e2484, 2023.
698

699 De Vrese, P., Georgievski, G., Gonzalez Rouco, J. F., Notz, D., Stacke, T., Steinert, N. J.,
700 Wilkenskjeld, S., and Brovkin, V.: Representation of soil hydrology in permafrost regions may
701 explain large part of inter-model spread in simulated Arctic and subarctic climate, *The Cryosphere*,
702 17, 2095–2118, <https://doi.org/10.5194/tc-17-2095-2023>, 2023.
703

704 Dominé, F., Fourteau, K., Picard, G., *et al.*: Permafrost cooled in winter by thermal bridging
705 through snow-covered shrub branches, *Nat. Geosci.*, 15, 554–560, [https://doi.org/10.1038/s41561-](https://doi.org/10.1038/s41561-022-00979-2)
706 [022-00979-2](https://doi.org/10.1038/s41561-022-00979-2), 2022.
707

708 Duchkov, A. D., Sokolova, L. S., Balobaev, V. T., Devyatkin, V. N., Kononov, V. I., and Lysak, S.
709 V.: Heat flow and geothermal field in Siberia, *Geologiya / Geofizika*, 38(11), 1716–1729, 1997.
710

711 Essery, R.: A factorial snowpack model (FSM 1.0), *Geosci. Model Dev.*, 8, 3867–3876,
712 <https://doi.org/10.5194/gmd-8-3867-2015>, 2015.
713

714 Eyring, V., Bony, S., Meehl, G. A., Senior, C. A., Stevens, B., Stouffer, R. J., and Taylor, K. E.:
715 Overview of the Coupled Model Intercomparison Project Phase 6 (CMIP6) experimental design and
716 organization, *Geosci. Model Dev.*, 9, 1937–1958, <https://doi.org/10.5194/gmd-9-1937-2016>, 2016.
717

718 Fan, X., Duan, Q., Shen, C., Wu, Y., and Xing, C.: Global surface air temperatures in CMIP6:
719 Historical performance and future changes, *Environ. Res. Lett.*, 15, 104056,
720 <https://doi.org/10.1088/1748-9326/abb051>, 2020.
721

722 Fedorov, A. N., Konstantinov, P. Y., Vasilyev, N. F., and Shestakova, A. A., The influence of
723 boreal forest dynamics on the current state of permafrost in Central Yakutia, *Polar Science*, 22,
724 100483, <https://doi.org/10.1016/j.polar.2019.100483>, 2019.
725

726 Frolking, S.: Sensitivity of spruce/moss boreal forest net ecosystem productivity to seasonal
727 anomalies in weather, *Journal of Geophysical Research*, 102(D24), 29053–29064,
728 <https://doi.org/10.1029/96JD03707>, 1997.
729

730 Gauthier, S., *et al.*: Boreal forest health and global change, *Science*, 349, 819–822,
731 <https://doi.org/10.1126/science.aaa9092>, 2015.
732

733 Gentsch, N.: Permafrost Soils in Central Siberia: Landscape Controls on Soil Organic Carbon
734 Storage in a Light Taiga Biome, Akademische Verlagsgemeinschaft München, Munich, Germany,
735 2011.
736

737 Haesen, S., Lembrechts, J. J., De Frenne, P., Lenoir, J., Aalto, J., Ashcroft, M. B., Kopecký, M.,
738 Luoto, M., Maclean, I., Nijs, I., Niittynen, P., van den Hoogen, J., Arriga, N., Brúna, J., Buchmann,
739 N., Čiliak, M., Collalti, A., De Lombaerde, E., Descombes, P., ... Van Meerbeek, K.: ForestTemp –
740 Sub-canopy microclimate temperatures of European forests, *Global Change Biology*, 27, 6307–
741 6319, <https://doi.org/10.1111/gcb.15892>, 2021.
742

743 Hamm, A., and Frampton, A.: Impact of lateral groundwater flow on hydrothermal conditions of the
744 active layer in a high-Arctic hillslope setting, *The Cryosphere*, 15, 4853–4871,
745 <https://doi.org/10.5194/tc-15-4853-2021>, 2021.
746

747 Hamon, W.R.: Computation of direct runoff amounts from storm rainfall, *International Association*
748 *of Scientific Hydrological Sciences Publication*, 63, 52–62, 1963.
749

750 Heijmans, M. M. P. D., Magnússon, R. Í. Lara, M. J., *et al.*: Tundra vegetation change and impacts
751 on permafrost, *Nat. Rev. Earth Environ.*, 3, 68–84, <https://doi.org/10.1038/s43017-021-00233-0>,
752 2022.
753

754 Hersbach, H., Bell, B., Berrisford, P., Hirahara, S., Horányi, A., Muñoz-Sabater, J., Nicolas, J.,
755 Peubey, C., Radu, R., Schepers, D., Simmons, A., Soci, C., Abdalla, S., Abellan, X., Balsamo, G.,
756 Bechtold, P., Biavati, G., Bidlot, J., Bonavita, M., De Chiara, G., Dahlgren, P., Dee, D.,
757 Diamantakis, M., Dragani, R., Flemming, J., Forbes, R., Fuentes, M., Geer, A., Haimberger, L.,
758 Healy, S., Hogan, R. J., Hólm, E., Janisková, M., Keeley, S., Laloyaux, P., Lopez, P., Lupu, C.,
759 Radnoti, G., de Rosnay, P., Rozum, I., Vamborg, F., Villaume, S., and Thépaut, J.-N.: The ERA5
760 global reanalysis, *Q. J. Roy. Meteor. Soc.*, 146, 1999–2049, <https://doi.org/10.1002/qj.3803>, 2020.
761

762 Hjort, J., Karjalainen, O., Aalto, J., *et al.*: Degrading permafrost puts Arctic infrastructure at risk by
763 mid-century, *Nat. Commun.*, 9, 5147, <https://doi.org/10.1038/s41467-018-07557-4>, 2018.
764

765 Hjort, J., Streletskiy, D., Doré, G., *et al.*: Impacts of permafrost degradation on infrastructure, *Nat.*
766 *Rev. Earth Environ.*, 3, 24–38, <https://doi.org/10.1038/s43017-021-00247-8>, 2022.
767

768 Hock, R.: Temperature index melt modelling in mountain areas, *Journal of Hydrology*, 282(1–4),
769 104–115, [https://doi.org/10.1016/S0022-1694\(03\)00257-9](https://doi.org/10.1016/S0022-1694(03)00257-9), 2003.
770

771 Holloway, J. E., Lewkowicz, A. G., Douglas, T. A., *et al.*: Impact of wildfire on permafrost
772 landscapes: A review of recent advances and future prospects, *Permafrost and Periglac. Process.*,
773 31, 371–382, <https://doi.org/10.1002/ppp.2048>, 2020.
774

775 Hu, G., Zhao, L., Wu, T., Wu, X., Park, H., Li, R., *et al.*: Continued warming of the permafrost
776 regions over the Northern Hemisphere under future climate change, *Earth’s Future*, 10,
777 e2022EF002835, <https://doi.org/10.1029/2022EF002835>, 2022.
778

779 Hu, G., Zhao, L., Li, R., Park, H., Wu, X., Su, Y., Guggenberger, G., Wu, T., Zou, D., Zhu, X.,
780 Zhang, W., Wu, Y., and Hao, J.: Water and heat coupling processes and its simulation in frozen
781 soils: Current status and future research directions, *CATENA*, 222, 106844, ISSN 0341-8162,
782 <https://doi.org/10.1016/j.catena.2022.106844>, 2023
783

784 Iturbide, M., Fernández, J., Gutiérrez, J. M., Bedia, J., Cimadevilla, E., Díez-Sierra, J., Manzanas,
785 R., Casanueva, A., Baño-Medina, J., Milovac, J., Herrera, S., Cofiño, A. S., San Martín, D., García-

786 Díez, M., Hauser, M., Huard, D., and Yelekci, Ö.: Repository supporting the implementation of
787 FAIR principles in the IPCC-WG1 Atlas, Zenodo, <https://doi.org/10.5281/zenodo.3691645>,
788 <https://github.com/IPCC-WG1/Atlas>, 2022.
789

790 Jan, A., and Painter, S. L.: Permafrost thermal conditions are sensitive to shifts in snow timing,
791 *Environ. Res. Lett.*, 15, 084026, 2020.
792

793 Jan, A.: Modeling the role of lateral surface flow in low-relief polygonal tundra, *Permafrost and*
794 *Periglac. Process.*, 33(3), 214–225, <https://doi.org/10.1002/ppp.2145>, 2022.
795

796 Ji, H., Nan, Z., Hu, J., Zhao, Y., and Zhang, Y.: On the spin-up strategy for spatial modeling of
797 permafrost dynamics: A case study on the Qinghai-Tibet Plateau, *Journal of Advances in Modeling*
798 *Earth Systems*, 14, e2021MS002750, <https://doi.org/10.1029/2021MS002750>, 2022.
799

800 Jin, H., Huang, Y., Bense, V. F., Ma, Q., Marchenko, S. S., Shepelev, V. V., Hu, Y., Liang, S.,
801 Spektor, V. V., Jin, X., *et al.*: Permafrost degradation and its hydrogeological impacts, *Water*, 14,
802 372, <https://doi.org/10.3390/w14030372>, 2022.
803

804 Karjalainen, O., Aalto, J., Luoto, M., *et al.*: Circumpolar permafrost maps and geohazard indices for
805 near-future infrastructure risk assessments, *Sci. Data*, 6, 190037,
806 <https://doi.org/10.1038/sdata.2019.37>, 2019.
807

808 Karlsson, J., Serikova, S., Vorobyev, S. N., *et al.*: Carbon emission from Western Siberian inland
809 waters. *Nat. Commun.*, 12, 825, <https://doi.org/10.1038/s41467-021-21054-1>, 2021.
810

811 Kim, J.-S., *et al.*: Extensive fires in southeastern Siberian permafrost linked to preceding Arctic
812 Oscillation, *Sci. Adv.*, 6, eaax3308, <https://doi.org/10.1126/sciadv.aax3308>, 2020.
813

814 Kirilyanov, A.V., Saurer, M., Siegwolf, R., Knorre, A. A., Prokushkin, A. S., Churakova
815 (Sidorova), O. V., Fonti M. V., and Büntgen, U.: Long-term ecological consequences of forest fires
816 in the continuous permafrost zone of Siberia, *Environ. Res. Lett.*, 15, 034061, 2020.
817

818 Kirdyanov, A.V., Saurer, M., Arzac, A., Knorre, A. A., Prokushkin, A. S., Churakova (Sidorova),
819 O. V., Arosio, T., Bebchuk, T., Siegwolf, R., and Büntgen, U.: Thawing permafrost can mitigate
820 warming-induced drought stress in boreal forest trees, *Science of the Total Environment*, 912,
821 168858, ISSN 0048-9697, <https://doi.org/10.1016/j.scitotenv.2023.168858>, 2024.

822

823 Khani, H. M., Kinnard, C., Gascoïn, S., and Lévesque, E.: Fine-scale environment control on
824 ground surface temperature and thaw depth in a High Arctic tundra landscape, *Permafrost and*
825 *Periglac. Process.*, 34(4), 467–480, <https://doi.org/10.1002/ppp.2203>, 2023.

826

827 Kurylyk, B. L., and Watanabe, K.: The mathematical representation of freezing and thawing
828 processes in variably-saturated, non-deformable soils, *Advances in Water Resources*, 60, 160–177,
829 ISSN 0309-1708, <https://doi.org/10.1016/j.advwatres.2013.07.016>, 2013.

830

831 Kurylyk, B. L.: Engineering challenges of warming, *Nat. Clim. Chang.*, 9, 807–808,
832 <https://doi.org/10.1038/s41558-019-0612-8>, 2019.

833

834 Lamontagne-Hallé, P., McKenzie, J. M., Kurylyk, B. L., and Zipper, S.C.: Changing groundwater
835 discharge dynamics in permafrost regions, *Environ. Res. Lett.*, 13, 084017, 2018.

836

837 Li, X.-Y., Jin, H.-J., Wang, H.-W., Marchenko, S. S., Shan, W., Luo, D.-L., He, R.-X., Spektor, V.,
838 Huang, Y.-D., Li, X.-Y., and Jia, N.: Influences of forest fires on the permafrost environment: A
839 review, *Advances in Climate Change Research*, 12(1), 48–65, ISSN 1674-9278,
840 <https://doi.org/10.1016/j.accre.2021.01.001>, 2021.

841

842 Li, G., Zhang, M., Pei, W., Melnikov, A., Khristoforov, I., Li, R., and Yu, F.: Changes in
843 permafrost extent and active layer thickness in the Northern Hemisphere from 1969 to 2018,
844 *Science of the Total Environment*, 804, 150182, ISSN 0048-9697,
845 <https://doi.org/10.1016/j.scitotenv.2021.150182>, 2022a.

846

847 Li, C., Wei, Y., Liu, Y., Li, L., Peng, L., Chen, J., *et al.*: Active layer thickness in the Northern
848 Hemisphere: Changes from 2000 to 2018 and future simulations, *Journal of Geophysical Research:*
849 *Atmospheres*, 127, e2022JD036785, <https://doi.org/10.1029/2022JD036785>, 2022b.

850

851 Loranty, M. M., Abbott, B. W., Blok, D., Douglas, T. A., Epstein, H. E., Forbes, B. C., Jones, B.
852 M., Kholodov, A. L., Kropp, H., Malhotra, A., Mamet, S. D., Myers-Smith, I. H., Natali, S. M.,
853 O'Donnell, J. A., Phoenix, G. K., Rocha, A. V., Sonnentag, O., Tape, K. D., and Walker, D. A.:
854 Reviews and syntheses: Changing ecosystem influences on soil thermal regimes in northern high-
855 latitude permafrost regions, *Biogeosciences*, 15, 5287–5313, [https://doi.org/10.5194/bg-15-5287-](https://doi.org/10.5194/bg-15-5287-2018)
856 2018, 2018.

857

858 Makarieva, O., Nesterova, N., Post, D. A., Sherstyukov, A., and Lebedeva, L.: Warming
859 temperatures are impacting the hydrometeorological regime of Russian rivers in the zone of
860 continuous permafrost, *The Cryosphere*, 13, 1635–1659, <https://doi.org/10.5194/tc-13-1635-2019>,
861 2019.

862

863 Mashukov, D. A., Benkova, A. V., Benkova, V. E., *et al.*: Radial growth and anatomic structure of
864 the trunk wood of healthy and stag-headed larch trees on permafrost, *Contemp. Probl. Ecol.*, 14,
865 767–774, <https://doi.org/10.1134/S1995425521070143>, 2021.

866

867 Miner, K. R., Turetsky, M. R., Malina, E., *et al.*: Permafrost carbon emissions in a changing Arctic,
868 *Nat. Rev. Earth Environ.*, 3, 55–67, <https://doi:10.1038/s43017-021-00230-3>, 2022.

869

870 Nitzbon, J., Krinner, G., Schneider von Deimling, T., Werner, M., and Langer, M.: First
871 quantification of the permafrost heat sink in the Earth's climate system, *Geophysical Research*
872 *Letters*, 50, e2022GL102053, <https://doi.org/10.1029/2022GL102053>, 2023.

873

874 Nitze, I., Grosse, G., Jones, B. M., *et al.*: Remote sensing quantifies widespread abundance of
875 permafrost region disturbances across the Arctic and Subarctic, *Nat. Commun.*, 9, 5423,
876 <https://doi.org/10.1038/s41467-018-07663-3>, 2018.

877

878 Obu, J., Westermann, S., Bartsch, A., Berdnikov, N., Christiansen, H. H., Dashtseren, A., Delaloye,
879 R., Elberling, B., Etzelmüller, B., Kholodov, A., Khomutov, A., Kääb, A., Leibman, M. O.,
880 Lewkowicz, A. G., Panda, S. K., Romanovsky, V., Way, R. G., Westergaard-Nielsen, A., Wu, T.,
881 Yamkhin, J., and Zou, D., Northern Hemisphere permafrost map based on TTOP modelling for

882 2000–2016 at 1 km² scale, *Earth-Science Reviews*, 193, 299–316, ISSN 0012-8252,
883 <https://doi.org/10.1016/j.earscirev.2019.04.023>, 2019.

884

885 Oehri, J., Schaepman-Strub, G., Kim, J. S., *et al.*: Vegetation type is an important predictor of the
886 arctic summer land surface energy budget, *Nat. Commun.*, 13, 6379,
887 <https://doi.org/10.1038/s41467-022-34049-3>, 2022.

888

889 O’Neill, B. C., Tebaldi, C., van Vuuren, D. P., Eyring, V., Friedlingstein, P., Hurtt, G., Knutti, R.,
890 Kriegler, E., Lamarque, J.-F., Lowe, J., Meehl, G. A., Moss, R., Riahi, K., and Sanderson, B. M.:
891 The Scenario Model Intercomparison Project (ScenarioMIP) for CMIP6, *Geosci. Model Dev.*, 9,
892 3461–3482, <https://doi.org/10.5194/gmd-9-3461-2016>, 2016.

893

894 Orgogozo, L., Prokushkin, A. S., Pokrovsky, O. S., Grenier, C., Quintard, M., Viers, J., and Audry,
895 S.: Water and energy transfer modeling in a permafrost-dominated, forested catchment of Central
896 Siberia: The key role of rooting depth, *Permafrost and Periglacial Processes*, 30, 75–89,
897 <https://doi.org/10.1002/ppp.1995>, 2019.

898

899 Orgogozo, L., Xavier, T., Oulbani, H., and Grenier, C.: Permafrost modelling with OpenFOAM®:
900 New advancements of the permaFoam solver, *Computer Physics Communications*, 282,
901 <https://doi.org/10.1016/j.cpc.2022.108541>, 2023.

902

903 Park, H., Tanoue, M., Sugimoto, A., Ichiyanagi, K., Iwahana, G., and Hiyama, T.: Quantitative
904 separation of precipitation and permafrost waters used for evapotranspiration in a boreal forest: A
905 numerical study using tracer model, *Journal of Geophysical Research: Biogeosciences*, 126,
906 e2021JG006645, <https://doi.org/10.1029/2021JG006645>, 2021.

907

908 Park, S. W., Kim, J. S., and Kug, J. S.: The intensification of Arctic warming as a result of CO₂
909 physiological forcing, *Nat. Commun.*, 11, 2098, <https://doi.org/10.1038/s41467-020-15924-3>, 2020.

910

911 Park, S. W., and Kug, J. S.: A decline in atmospheric CO₂ levels under negative emissions may
912 enhance carbon retention in the terrestrial biosphere, *Commun. Earth Environ.*, 3, 289,
913 <https://doi.org/10.1038/s43247-022-00621-4>, 2022.

914

915 Pokrovsky, O. S., Schott, J. S., Kudryavtzev, D. I., and Dupré, B.: Basalt weathering in Central
916 Siberia under permafrost conditions, *Geochimica et Cosmochimica Acta*, 69(24), 5659–5680, 2005.

917

918 Porter, C., Howat, I., Noh, M.-J., Husby, E., Khuvis, S., Danish, E., Tomko, K., Gardiner, J.,
919 Negrete, A., Yadav, B., Klassen, J., Kelleher, C., Cloutier, M., Bakker, J., Enos, J., Arnold, G.,
920 Bauer, G., and Morin, P., ArcticDEM - Mosaics, Version 4.1, Harvard Dataverse, V1,
921 <https://doi.org/10.7910/DVN/3VDC4W>, 2023.

922

923 Prokushkin, A., Kajimoto, T., Prokushkin, S., McDowell, W., Abaimov, A. P., and Matsuura, Y.:
924 Climatic factors influencing fluxes of dissolved organic carbon from the forest floor in a
925 continuous-permafrost Siberian watershed, *Canadian Journal of Forest Research-Journal Canadien
de la Recherche Forestiere*, 35, 2130–2140, <https://doi.org/10.1139/x05-150>, 2004.

927

928 Prokushkin, A. S., Gleixner, G., McDowell, W. H., Ruehlow, S., and Schulze, E.-D.: Source- and
929 substrate-specific export of dissolved organic matter from permafrost-dominated forested watershed
930 in central Siberia, *Global Biogeochem. Cycles*, 21, GB4003,
931 <https://doi.org/10.1029/2007GB002938>, 2007.

932

933 Ramage, J., Jungsberg, L., Wang, S., *et al.*: Population living on permafrost in the Arctic, *Popul.
934 Environ.*, 43, 22–38, <https://doi.org/10.1007/s11111-020-00370-6>, 2021.

935

936 Revich, B. A., Eliseev, D. O., and Shaposhnikov, D. A.: Risks for public health and social
937 infrastructure in Russian Arctic under climate change and permafrost degradation, *Atmosphere*, 13,
938 532, <https://doi.org/10.3390/atmos13040532>, 2022.

939

940 Rew, L. J., McDougall, K. L., Alexander, J. M., Daehler, C. C., Essl, F., Haider, S., Kueffer, C.,
941 Lenoir, J., Milbau, A., Nuñez, M. A., Pauchard, A., and Rabitsch, W.: Moving up and over:
942 Redistribution of plants in alpine, Arctic, and Antarctic ecosystems under global change, *Arctic,
943 Antarctic, and Alpine Research*, 52(1), 651–665, <https://doi.org/10.1080/15230430.2020.1845919>,
944 2020.

945

946 Schneider von Deimling, T., Lee, H., Ingeman-Nielsen, T., Westermann, S., Romanovsky, V.,
947 Lamoureux, S., Walker, D. A., Chadburn, S., Trochim, E., Cai, L., Nitzbon, J., Jacobi, S., and
948 Langer, M.: Consequences of permafrost degradation for Arctic infrastructure – bridging the model
949 gap between regional and engineering scales, *The Cryosphere*, 15, 2451–2471,
950 <https://doi.org/10.5194/tc-15-2451-2021>, 2021.
951

952 Schuur, E.A.G., *et al.*: Permafrost and climate change: Carbon cycle feedbacks from the warming
953 Arctic, *Annual Review of Environment and Resources*, 47(1), 343–371, 2022.
954

955 Shiklomanov, N. I., Streletskiy, D. A., Swales, T. B., and Kokorev, V. A.: Climate change and
956 stability of urban infrastructure in Russian permafrost regions: Prognostic assessment based on
957 GCM climate projections, *Geographical Review*, 107(1), 125–142,
958 <https://doi.org/10.1111/gere.12214>, 2017.
959

960 Sjöberg, Y., Coon, E., Sannel, A. B. K., Pannetier, R., Harp, D., Frampton, A., Painter, S. L., and
961 Lyon, S. W.: Thermal effects of groundwater flow through subarctic fens: A case study based on
962 field observations and numerical modeling, *Water Resour. Res.*, 52, 1591–1606,
963 <https://doi.org/10.1002/2015WR017571>, 2016.
964

965 Sonke, J. E., Teisserenc, R., Heimbürger-Boavida, L.-E., Petrova, M. V., Maruszczak, N., Le Dantec,
966 T., Chupakov, A. V., Li, C., Thackray, C. P., Sunderland, E. M., Tananaev, N., and Pokrovsky, O.
967 S.: Eurasian river spring flood observations support net Arctic Ocean mercury export to the
968 atmosphere and Atlantic Ocean, *PNAS*, 115, 50, E11586–E11594,
969 www.pnas.org/cgi/doi/10.1073/pnas.1811957115, 2018.
970

971 Speetjens, N. J., Hugelius, G., Gumbrecht, T., Lantuit, H., Berghuijs, W. R., Pika, P. A., Poste, A.,
972 and Vonk, J. E.: The pan-Arctic catchment database (ARCADE), *Earth Syst. Sci. Data*, 15, 541–
973 554, <https://doi.org/10.5194/essd-15-541-2023>, 2023.
974

975 Streletskiy, D. A., Suter, L. J., Shiklomanov, N. I., Porfiriev, B. N., and Eliseev, D. O.: Assessment
976 of climate change impacts on buildings, structures and infrastructure in the Russian regions on
977 permafrost, *Environ. Res. Lett.*, 14, 025003, 2019.
978

979 Streletskiy, D. A., Clemens, S., Lanckman, J.-P., and Shiklomanov, N. I.: The costs of Arctic
980 infrastructure damages due to permafrost degradation, *Environ. Res. Lett.*, 18, 015006,
981 <https://doi.org/10.1088/1748-9326/acab18>, 2023.
982

983 Stuenzi, S. M., Boike, J., Gädeke, A., Herzsuh, U., Kruse, S., Pestryakova, L. A., Westermann,
984 S., and Langer, M.: Sensitivity of ecosystem-protected permafrost under changing boreal forest
985 structures, *Environ. Res. Lett.*, 16, 084045, <https://doi.org/10.1088/1748-9326/ac153d>, 2021.
986

987 van Vuuren, D. P., Edmonds, J., Thomson, A., Riahi, K., Kainuma, M., Matsui, T., Hurtt, G. C.,
988 Lamarque, J.-F., Meinshausen, M., Smith, S., Granier, C., Rose, S. K., and Hibbard, K. A.: The
989 representative concentration pathways: An overview, *Climatic Change*, 109, 5–31,
990 <https://doi.org/10.1007/s10584-011-0148-z>, 2011.
991

992 Viers, J., Prokushkin, A. S., Pokrovsky, O. S., *et al.*: Seasonal and spatial variability of elemental
993 concentrations in boreal forest larch foliage of Central Siberia on continuous permafrost,
994 *Biogeochemistry*, 113(1-3), 435–449, <https://doi.org/10.1007/s10533-012-9770-8>, 2013.
995

996 Vitasse, Y., Porté, A. J., Kremer, A., *et al.*: Responses of canopy duration to temperature changes in
997 four temperate tree species: Relative contributions of spring and autumn leaf phenology, *Oecologia*,
998 161, 187–198, <https://doi.org/10.1007/s00442-009-1363-4>, 2009.
999

1000 Vitasse, Y., François, C., Delpierre, N., Dufrêne, E., Kremer, A., Chuine, I., and Delzon S.:
1001 Assessing the effects of climate change on the phenology of European temperate trees, *Agricultural*
1002 *and Forest Meteorology*, 151(7), 969–980, ISSN 0168-1923,
1003 <https://doi.org/10.1016/j.agrformet.2011.03.003>, 2011.
1004

1005 Vonk, J. E., Speetjens, N. J., and Poste, A. E.: Small watersheds may play a disproportionate role in
1006 arctic land-ocean fluxes, *Nat. Commun.*, 14, 3442, <https://doi.org/10.1038/s41467-023-39209-7>,
1007 2023.
1008

1009 Walvoord, M. A., and Kurylyk, B. L.: Hydrologic impacts of thawing permafrost—A review,
1010 *Vadose Zone Journal*, 15, 1–20, <https://doi.org/10.2136/vzj2016.01.0010>, 2016.
1011

1012 Walvoord, M. A., and Striegl, R. G.: Complex vulnerabilities of the water and aquatic carbon cycles
1013 to permafrost thaw, *Front. Clim.*, 3, 730402, <https://doi.org/10.3389/fclim.2021.730402>, 2021.
1014

1015 Wang, J., and Liu, D.: Vegetation green-up date is more sensitive to permafrost degradation than
1016 climate change in spring across the northern permafrost region, *Global Change Biology*, 28, 1569–
1017 1582, <https://doi.org/10.1111/gcb.16011>, 2022.

1018

1019 Weller, H. G., Tabor, G., Jasak, H., and Fureby, C.: A tensorial approach to computational
1020 continuum mechanics using object orientated techniques, *Computers in Physics*, 12, 620–631,
1021 <https://doi.org/10.1063/1.168744>, 1998.

1022

1023 Westermann, S., Barboux, C., Bartsch, A., Delaloye, R., Grosse, G., Heim, B., Hugelius, G.,
1024 Irrgang, A., Kääh, A. M., Matthes, H., Nitze, I., Pellet, C., Seifert, F. M., Strozzi, T., Wegmüller,
1025 U., Wieczorek, M., and Wiesmann, A.: ESA Permafrost Climate Change Initiative
1026 (Permafrost_cci): Permafrost active layer thickness for the Northern Hemisphere, v4.0, NERC EDS
1027 Centre for Environmental Data Analysis, 24 April 2024,
1028 <https://doi.org/10.5285/d34330ce3f604e368c06d76de1987ce5>, 2024.

1029

1030 Wright, S. N., Thompson, L. M., Olefeldt, D., Connon, R. F., Carpino, O. A., Beel, C. R., and
1031 Quinton, W. L.: Thaw-induced impacts on land and water in discontinuous permafrost: A review of
1032 the Taiga Plains and Taiga Shield, northwestern Canada, *Earth-Science Reviews*, 232, 104104,
1033 ISSN 0012-8252, <https://doi.org/10.1016/j.earscirev.2022.104104>, 2022.

1034

1035 Zellweger, F., Coomes, D., Lenoir, J., *et al.*: Seasonal drivers of understory temperature buffering
1036 in temperate deciduous forests across Europe, *Global Ecol. Biogeogr.*, 28, 1774–1786,
1037 <https://doi.org/10.1111/geb.12991>, 2019.

1038

1039 Zellweger, F., *et al.*: Forest microclimate dynamics drive plant responses to warming, *Science*, 368,
1040 772–775, <https://doi.org/10.1126/science.aba6880>, 2020.